



## Article

# New Insights into Surface Deposits in the Balmer-Kapteyn Cryptomare Region Provided by Chang'E-2 Microwave Radiometer Data

Tianqi Tang <sup>1,2</sup>, Zhiguo Meng <sup>1,2,\*</sup>, Yi Lian <sup>3</sup>, Zhiyong Xiao <sup>4</sup>, Jingsong Ping <sup>5,6</sup>, Zhanchuan Cai <sup>2</sup>, Xiaoping Zhang <sup>2</sup>, Xuegang Dong <sup>1</sup> and Yuanzhi Zhang <sup>5,6</sup>

<sup>1</sup> College of Geoexploration Science and Technology, Jilin University, Changchun 130026, China

<sup>2</sup> State Key Laboratory of Lunar and Planetary Sciences, Macau University of Science and Technology, Macau 999078, China

<sup>3</sup> College of Geographic and Environmental Sciences, Tianjin Normal University, Tianjin 300387, China

<sup>4</sup> Planetary Environmental and Astrobiological Research Laboratory, School of Atmospheric Sciences, Sun Yat-sen University, Zhuhai 519000, China

<sup>5</sup> Key Laboratory of Lunar and Deep-Space Exploration, National Astronomical Observatories, Chinese Academy of Sciences, Beijing 100101, China

<sup>6</sup> School of Astronomy and Space Science, University of Chinese Academy of Sciences, Beijing 100049, China

\* Correspondence: mengzg@jlu.edu.cn; Tel.: +86-186-4306-2191

**Abstract:** Lunar cryptomare records both early-stage mare volcanisms and large-scale impact cratering, which can provide important information about the thermal evolution of the Moon. We built a mixing dielectric constant model to represent the cryptomare deposits mixed by highland debris and mare deposits, and the proper radiative transfer simulation was constructed to evaluate the thermal emission features of surface deposits in the cryptomare region. The microwave radiometer (MRM) data in the Balmer-Kapteyn region were extracted, and the linear interpolation method was used to generate brightness temperature (TB) maps at noon and at night. To enhance the correlation between cryptomare deposits and TB performances, normalized TB (nTB) and TB difference (dTB) maps were also generated. Combined with the datasets, including Lunar Reconnaissance Orbiter Wide Angle Camera, Lunar Orbiter Laser Altimeter, and Diviner and Clementine UV-VIS, the main findings are as follows: (1) The mare-like cryptomare deposits were discovered and identified according to the nTB and dTB performances. Combined with the surface compositions, at least two kinds of buried mare deposits were identified in the B-K region, which erupted during different episodes. (2) A construct-like volcanic feature was suggested by the nTB and dTB performances. (3) The results of our analysis indicated the presence of materials with low dTB anomalies in the northern and southwestern parts of the cryptomare region and in the mare unit within the Vendelinus crater, which illustrates the heterogeneity of the lunar crust in the vertical direction.

**Keywords:** Balmer-Kapteyn cryptomare region; Chang'E-2 microwave radiometer; surface deposits; microwave thermal emission; brightness temperature



**Citation:** Tang, T.; Meng, Z.; Lian, Y.; Xiao, Z.; Ping, J.; Cai, Z.; Zhang, X.; Dong, X.; Zhang, Y. New Insights into Surface Deposits in the Balmer-Kapteyn Cryptomare Region Provided by Chang'E-2 Microwave Radiometer Data. *Remote Sens.* **2022**, *14*, 4556. <https://doi.org/10.3390/rs14184556>

Academic Editor: Christian Wöhler

Received: 4 July 2022

Accepted: 8 September 2022

Published: 12 September 2022

**Publisher's Note:** MDPI stays neutral with regard to jurisdictional claims in published maps and institutional affiliations.



**Copyright:** © 2022 by the authors. Licensee MDPI, Basel, Switzerland. This article is an open access article distributed under the terms and conditions of the Creative Commons Attribution (CC BY) license (<https://creativecommons.org/licenses/by/4.0/>).

## 1. Introduction

Cryptomare is composed of mare basalt deposits that were buried or obscured by higher albedo materials ejected from basins or craters [1,2]. Cryptomare was formed by early basaltic volcanism primarily from 3.8 Ga to 4.35 Ga, and its formation history is critical for better understanding the lunar thermal and volcanic evolution, mantle convection, and magma ocean solidification of the Moon [2–7]. Thus, the identification of cryptomare is always an important objective of lunar study.

The major defining criteria of the cryptomare region are the ancient mare basalt deposits covered by later impact ejecta, which were then excavated by an impact cratering process. The size and distance of the crater or basin assumed to be the source of the ejecta

can be used to classify cryptomare into four types: Copernicus-type, Balmer-type, Proximal basin ejecta-type, and Distal basin ejecta-type [2,5]. In previous studies, the identification of cryptomare deposits had been mainly based on the presence of a dark-haloed crater (DHC) with the impact origin, exposing the mare deposits underlying the surface ejecta and distributed around the crater as a dark halo [6,8,9]. The distribution of the DHC is employed to delineate the range of the cryptomare region [2,10]. However, the main challenge for identifying the cryptomare region is the shadow effect, which may create the visible “dark halo” and lead to the misidentification of DHC in visible images [11]. Moreover, space weathering also presents a challenge for identifying DHCs, because this process alternates surface albedo with time [12]. Schultz and Spudis [3] noted that the albedo contrasts between impact melts and ejecta deposits decrease rapidly with time, resulting in the misidentification of impact melts as basaltic dark halos. Thus, it is difficult to completely map the cryptomare region with the optical data.

To aid in identifying surface deposits in the cryptomare region, the geochemical and mineralogical anomalies are introduced [2,4,6,7,13,14]. Based on Fe concentrations derived from the data from the Apollo gamma-ray spectrometer (GRS) [15], Antonenko et al., [2] noted that Fe values were higher in the cryptomare region than in its vicinity. In addition, using the half-degree FeO abundance reckoned with lunar prospector (LP) GRS data during the low-altitude portion of the mission [16], it was suggested that the surface deposits have a strong correlation with the enhanced FeO values in the typical cryptomare regions as the Lomonosov-Fleming (L-F), Schiller-Schickard (S-S), Mendel-Rydberg (M-R), and Balmer-Kapteyn (B-K) regions [3,5,17,18], whereas the ability to identify surface deposits in the cryptomare region is still limited with GRS data for the poor spatial resolution.

New methods have been explored to evaluate the surface deposits in the cryptomare region. Campbell and Hawke [9] outlined the extent of the cryptomare region in the east of the Orientale basin using ground-based radar data. Sori et al., [19] attempted to assess the relationship between the positive Bouguer gravity anomalies and the cryptomare region with Gravity Recovery and Interior Laboratory (GRAIL) data. The development of new data sources and analysis methods is indispensable for studying the nature of the surface deposits in cryptomare regions.

In China’s Chang’E (CE)-1/2 missions, a microwave radiometer (MRM) was brought onboard the satellite to passively measure the brightness temperature (TB) of the regolith. The penetration depths of the MRM data can be up to several meters below the surface [20,21]. The sensitivity of MRM data to the thermal emission features of the regolith at the penetration depth has been proven; the data provide a good description of the surface deposits in the vertical direction [21–23]. Combining the data from the Lunar Reconnaissance Orbiter (LRO) Diviner data and the Lunar Orbiter Laser Altimeter data, Siegler et al., [24] and Feng et al., [25] also suggested that the CE-2 MRM data are sensitive to the loss tangent of the regolith, which is positively correlated with the ilmenite content of the substrate materials on the lunar surface [26]. Thus, MRM data provide a new way to assess the distribution and dielectric properties of cryptomare deposits, which was the motivation for this study.

Until now, cryptomare deposits have been discovered in the Balmer-Kapteyn (B-K), Schiller-Schickard, Lomonosov-Fleming, and Mendel-Rydberg regions, exhibiting extensive and continuous distribution [6]. The cryptomare deposits in the B-K region have been thoroughly studied with multiple spacecraft images, including Lunar Orbiter data, Clementine multispectral data, and LP-GRS data [5,7]. Therefore, the B-K region was selected as the study area to evaluate the use of MRM data for identifying cryptomare deposits. Some new viewpoints on the following questions are proposed: (1) Can the CE-2 MRM data identify cryptomare deposits in the B-K region? (2) What are the microwave thermal emission features of the surface deposits in the cryptomare region? (3) What geological implications can potentially be postulated by MRM data with penetration ability in the cryptomare region?

## 2. Numerical Simulation

To better understand the TB performances of the deposits in the cryptomare region, a layered regolith model and the corresponding microwave radiative transfer equations are constructed in this section.

### 2.1. Radiative Transfer Simulation of Cryptomare Deposits

When studying the TB performances of cryptomare deposits, it is important to first construct a proper layered regolith model. Until now, the commonly used models have been the two-layer models, including the regolith and the rock layers [22,27–29].

In the B-K region, the thickness of the surface impact ejecta in the cryptomare region is at least 33 m [7], which is beyond the penetration depth of the microwave used by the MRM instrument. Thus, a one-layer model with infinite depth is employed to construct the radiative transfer model, which is an extension of the two-layer model (Figure 1a) [24,25,30].

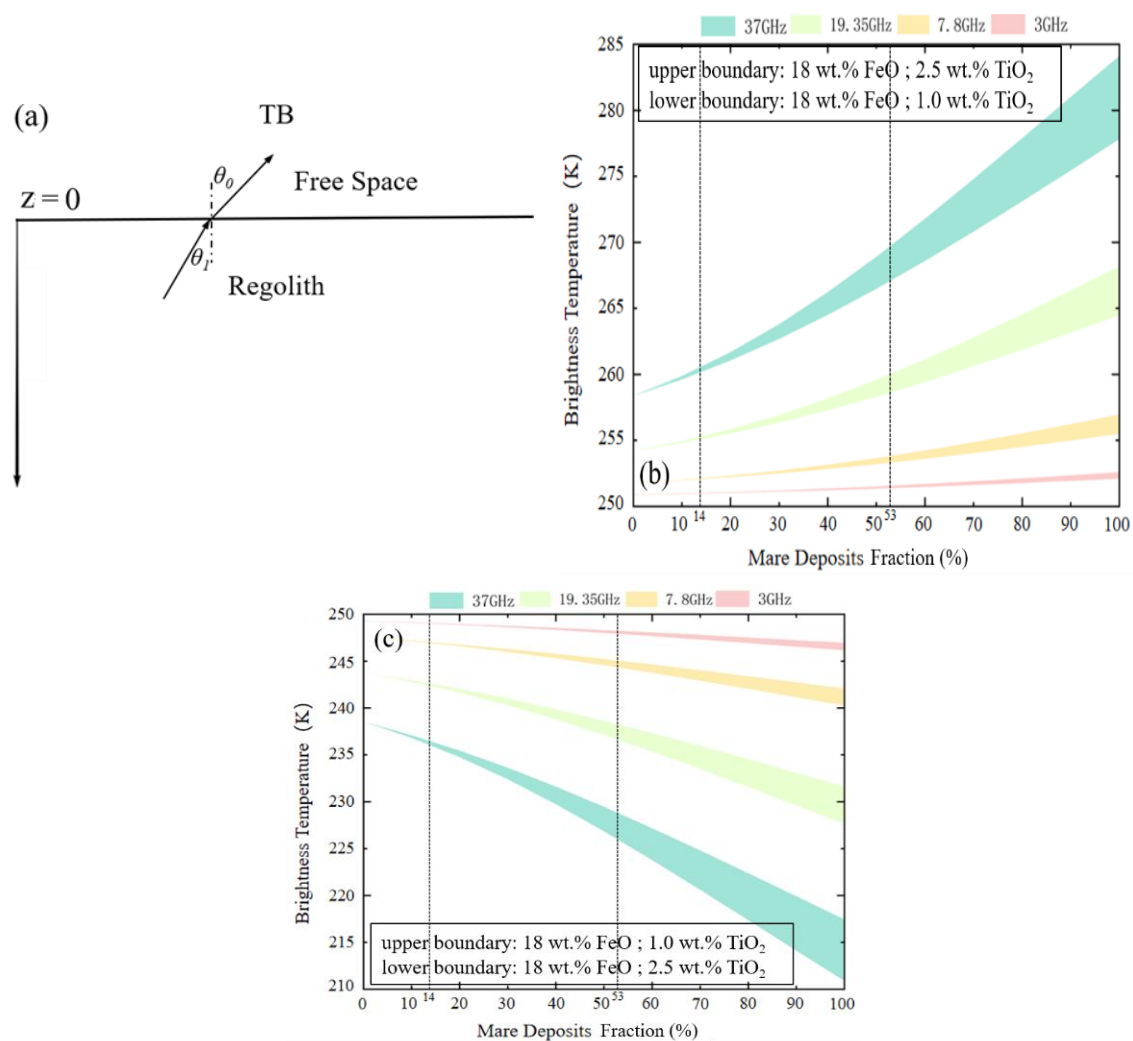


**Figure 1.** (a) The constructed one-layer regolith model with infinite depth proper for cryptomare deposits. (b) Model brightness temperature vs. mare deposit fraction for the Chang'E-2 MRM frequencies at noon (11 o'clock). The upper boundary of every belt is the mare deposit with 18 wt.% FeO and 2.5 wt.% TiO<sub>2</sub>, and the lower boundary is the mare deposit with 18 wt.% FeO and 1.0 wt.% TiO<sub>2</sub>. (c) Model brightness temperature vs. mare deposit abundance fraction for the Chang'E-2 MRM frequencies at night (22 o'clock). The upper boundary of every belt is the mare deposit with 18 wt.% FeO and 1.0 wt.% TiO<sub>2</sub> and the lower boundary is the mare deposit with 18 wt.% FeO and 2.5 wt.% TiO<sub>2</sub>.

An expression for the model is as follows [30]:

$$dT B_p = (1 - r_p)k_\alpha(z)T(z)\sec\theta_1 e^{-\int_0^z k_\alpha(z')\sec\theta_1 dz'} dz \tag{1}$$

where  $\theta_0$  and  $\theta_1$  are the incident angles, as shown in Figure 1a;  $r_p$  is the reflectivity of the free air and the regolith layer interface,  $p = h; v$  represents the horizontal or vertical polarization, which is expressed as:

$$r_h = \left| \frac{\cos\theta_1 - \sqrt{\epsilon_1 - \sin^2\theta_1}}{\cos\theta_1 + \sqrt{\epsilon_1 - \sin^2\theta_1}} \right|^2 \tag{2}$$

$$r_v = \left| \frac{\epsilon_1 \cos\theta_1 - \sqrt{\epsilon_1 - \sin^2\theta_1}}{\epsilon_1 \cos\theta_1 + \sqrt{\epsilon_1 - \sin^2\theta_1}} \right|^2 \tag{3}$$

where  $\epsilon_1$  is the relative dielectric constant of the regolith.

$K_\alpha(z)$  is the absorption coefficient of the regolith, which is given by:

$$k_\alpha(z) = 2Im(2\pi f \sqrt{\mu_0 \epsilon_1 \epsilon_0}) \tag{4}$$

where  $f$  is the frequency;  $\mu_0$  stands for the vacuum permeability;  $\epsilon_0$  stands for the dielectric constants of the vacuum.

The dielectric constant of the regolith is a key parameter for obtaining the reflectivity and absorption coefficient and is essential for evaluating the cryptomare deposits. After studying the excavated mare deposits surrounding the DHCs, Hawke et al., [5] suggested that dark halos may be contaminated by variable amounts of highland debris. Thus, considering the widely distributed impact craters and the degradation of DHCs, we hypothesize that the cryptomare deposits are a mixture of highland debris and mare deposits. Additionally, enhanced ferrous abundances are thought to be the key measure for identifying cryptomare deposits, indicating that the mixture of the highland debris and the mare deposits is widely distributed in the cryptomare region [5,6]. The mixing model for the dielectric constants developed by Berryman [31] is employed in this study; it was also used by Hu et al., [32] to evaluate the dielectric constant of regolith mixing with rocks. The expression is expressed as follows.

$$\frac{\epsilon_{\text{mare}} - \epsilon_1}{\epsilon_{\text{mare}} + 2\epsilon_1} * v + \frac{\epsilon_{\text{highland}} - \epsilon_1}{\epsilon_{\text{highland}} + 2\epsilon_1} * (1 - v) = 0 \tag{5}$$

where  $v$  stands for the fraction of the mare deposits;  $\epsilon_{\text{mare}}$  and  $\epsilon_{\text{highland}}$  are the dielectric constants of the mare deposits and the highland debris, respectively, which comprise the real part  $\epsilon'_{\text{mare}}$  and  $\epsilon'_{\text{highland}}$  and the imaginary part  $\epsilon''_{\text{mare}}$  and  $\epsilon''_{\text{highland}}$ . The dielectric constant model proposed by Carrier et al., is widely used in calculating the dielectric properties of the regolith [22,23,33], which is also used in this study as follows [26]:

$$\begin{cases} \epsilon' = 1.919\rho(z) \\ \epsilon'' = \epsilon' \times 10^{0.0385+0.312\rho(z)-3.260} \end{cases} \tag{6}$$

where  $S$  is the (FeO + TiO<sub>2</sub>) abundance (wt.%). The real part of the dielectric constant  $\epsilon'$  is determined by the deposit density,  $\rho$ , where the hyperbolic density model is employed and is similar to the mare deposits and highland debris. The main difference is in the imaginary part  $\epsilon''$ , where the  $S$  of mare deposits is much higher than that of highland debris.

$T(z)$  is the temperature profile in the regolith, obtained by solving the thermal conduction model [29]. The 1-D thermal conduction model describes the relationship between the dynamic temperature distribution  $T(z,t)$  (K) and the density  $\rho(z,T)$  (kg m<sup>-3</sup>), heat capac-

ity  $c(z,T)$  ( $\text{W kg}^{-1} \text{K}^{-1}$ ), and thermal conductivity  $K(z,T)$  ( $\text{W m}^{-1} \text{K}^{-1}$ ) of a semi-infinite medium, which is expressed as follows.

$$\rho(z,T)C(z,T)\frac{\partial T}{\partial t} = \frac{\partial}{\partial z} \left[ K(z,T)\frac{\partial T}{\partial z} \right] \quad (7)$$

where  $t$  represents the time.

Information about the cryptomare deposits in the vertical direction has been limited, and we assume that the mixing of highland debris and mare deposits is homogeneous, at least within the penetration depth of the MRM microwave. According to the TB performances in Regions C and R (two typical regions mentioned in Section 4.2), as shown in the following Figures, this assumption is reasonable.

## 2.2. Simulation Results of Cryptomare Deposits

The observation angle of the MRM instrument is  $0^\circ$  [20,21]; that is,  $\theta_0$  and  $\theta_1$  are both  $0^\circ$ . Assuming that uncontaminated buried mare deposits average 18 wt.% FeO and 1.0 wt.% to 2.5 wt.%  $\text{TiO}_2$  and that the local highlands average 5.2 wt.% FeO and 0.5 wt.%  $\text{TiO}_2$  (which is assessed by Hawke et al., [5]), the change in TB with the mixing fraction of mare deposits and highland debris can be simulated using Equation (1) (Figure 1b,c).

Figure 1b shows the change in the simulated TB with the mixing fraction at noon, and Figure 1c shows it at night. Here, the upper boundary at noon and the lower boundary at night are the simulated TB with 18 wt.% FeO and 2.5 wt.%  $\text{TiO}_2$ , and the lower boundary at noon and the upper boundary at night are the simulated TB with 18 wt.% FeO and 1.0 wt.%  $\text{TiO}_2$  at the TB belt of each frequency.

Figure 1b,c provide a new description of the TB performances of cryptomare deposits as follows. With the increase in the mare deposit fraction, TB increases at noon and decreases at night. The daytime TB at high frequency is higher than that at low frequency, while the nighttime TB at high frequency is lower than that at low frequency. This is a normal feature of TB in mare deposits, similarly as TB performances in Mare Imbrium and Mare Rümker regions [22,34]. Moreover, the nighttime TB in the cryptomare region with mixed mare deposits and highland debris should be lower than that in highland debris but higher than that in pure mare deposits and vice versa at daytime. The higher TB of mare deposit at noon and lower TB during the night compared with the highland debris agree well with the calculated thermal properties by Feng et al., [25], who proposed that the loss tangent of the dielectric constant of the surface deposits is higher in the maria than in the highlands.

This point is important for understanding the TB performances of the surface deposits in the B-K region and the findings regarding the mare-like cryptomare deposits and special materials with strong heat capacity in the following discussions.

Hawke et al., [5] concluded that the surfaces of the cryptomare deposits in the B-K region contain 14% to 53% mare deposits. Figure 1b,c show that in this mare deposit fraction range, the noon TB monotonously increases approximately 0.4–0.6 K at 3.0 GHz, 1.3–1.7 K at 7.8 GHz, 3.5–4.7 K at 19.35 GHz, and 6.9–9.0 K at 37 GHz, while the nighttime TB monotonously decreases by approximately 0.8–1.1 K at 3.0 GHz, approximately 2–2.6 K at 7.8 GHz, approximately 4.4–5.7 K at 19.35 GHz, and approximately 7.7–10 K at 37 GHz. Therefore, the cryptomare deposits can theoretically be detected by the MRM instrument. However, using the Chandrayaan-1 Moon Mineralogy Mapper ( $\text{M}^3$ ) data, Whitten and Head [6] found that many cryptomare regions did not have an enhanced mafic signature in the regolith because thicker ejecta deposits prevented substantial vertical mixing between the superposed ejecta and the underlying volcanic unit [35]. This would be an issue for evaluating cryptomare deposits with MRM data.

Moreover, Fang and Fa [36], Hu et al., [32], and Meng et al., [33] suggested that MRM data are strongly influenced by surface topography and rock abundances, in addition to the mafic fraction of the surface materials. Thus, the evaluation of cryptomare deposits with MRM data should be seriously considered.

### 2.3. Penetration Depth

Since the brightness temperature from the lunar surface is the cumulative contribution of thermal emission at different depths, the penetration depth is important for analyzing the observed TB [37]. The penetration depth of the microwave depends primarily on its wavelength and the complex dielectric constant of the lunar regolith, which can be expressed as follow [37,38]:

$$d_0 = \frac{\lambda\sqrt{\epsilon''}}{2\pi\epsilon''} \tag{8}$$

where  $d_0$  represents the penetration depth;  $\lambda$  is the wavelength.

Thus, Fa [37] suggested that the penetration depth is about 5 to 17 times of the used wavelength in maria regions, with an average value of about 10. Moreover, when studying the lunar surface using the ground-based radar, Campbell et al., [39] proposed that the penetration depth of the microwave signals is about 10 to 20 times of the used wavelength, which depends on the (FeO + TiO<sub>2</sub>) abundance of the surface deposits.

Thus, the penetration depth of the microwave signal is about 10 to 20 times of the used wavelength in the B-K region. The wavelength of the microwave used by the MRM instrument is 10 cm at 3.0 GHz, 3.85 cm at 7.8 GHz, 1.55 cm at 19.35 GHz, and 0.81 cm at 37 GHz. Correspondingly, the penetration depth is about 1 m to 2 m at 3.0 GHz, 38.5 cm to 75 cm at 7.8 GHz, 15.5 cm to 31 cm at 19.35 GHz, and 8.1 cm to 16.2 cm at 37 GHz, which is decided by the (FeO + TiO<sub>2</sub>) abundance (FTA) of the lunar regolith.

The penetration depths of the wavelength well postulate the TB behaviors, e.g., the TB variations are higher at 37 GHz than those at other channels, because the microwave at 37 GHz has a lower penetration depth. Correspondingly, the 37-GHz TB is sensitive to the regolith parameters in the top layers, including the surface temperatures, through a whole lunation.

## 3. Data Processing

### 3.1. Study Area and Regional Geology

The B-K region, ranging from 8°S to 28°S and from 60°E to 76°E, is located east of Mare Fecunditatis (Figure 2a). The B-K region is a pre-Nectarian impact structure with two topographic rings, approximately 225 km and 450 km in diameter, respectively [5].

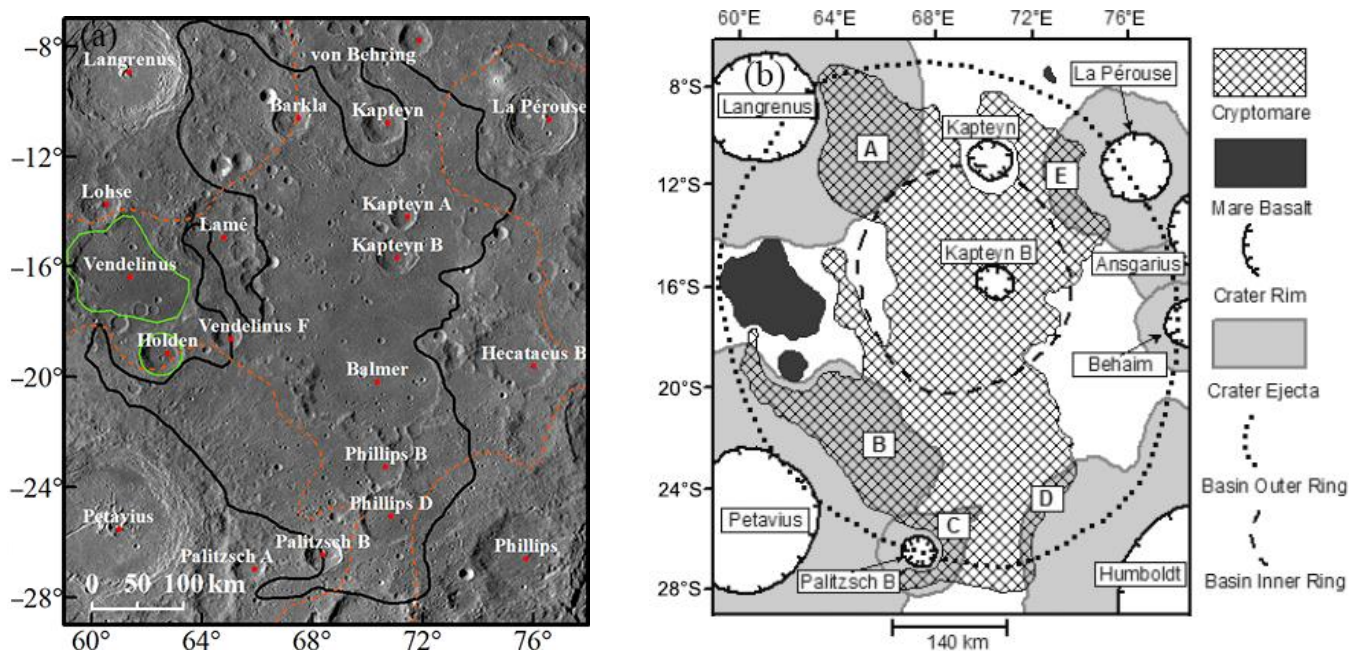


**Figure 2.** (a) A mosaic of the Wide-Angle Camera (WAC) image of the B-K region. The black line denotes the cryptomare unit, the green line denotes the mare unit, and the orange dashed line denotes

the ejecta interpreted by Hawke et al., [5], as shown in Figure 2b. (b) Sketch geological map of the B-K region [5]. Major expanses of cryptomare are covered by the continuous ejecta of Langrenus, Petavius, Palitzsch B, Humboldt, and La Pérouse craters, which are indicated by A, B, C, D, and E, respectively.

The B-K region contains one of the largest cryptomare deposits [5,6] on the Moon. Noting the presence of DHCs, the association with mafic geochemical anomalies, and the presence of a significant component of mare basalt in high-albedo surface units, Hawke et al., [5] determined the distribution and extent of the cryptomare deposits in the B-K region (Figure 2b). All the cryptomare regions are located within the outer ring of the B-K basin in a cross-hatched pattern, and the inner ring is wholly underlined by the mare deposits. The B-K cryptomare region was mainly formed by basin impact ejecta, including Mare Serenitatis and Mare Smythii [6]. Additionally, the cryptomare surfaces in the northern portion were contaminated by discontinuous highland-rich ejecta from the Langrenus (61.0°E, 8.9°S) and La Pérouse (76.3°E, 10.7°S) craters, while in the southern portion, the cryptomare surfaces were contaminated by highland-rich ejecta mainly from the Petavius (60.5°E, 25.2°S), Palitzsch B (68.4°E, 26.4°S), and Humboldt (81.0°E, 27.0°S) craters [5].

### 3.2. TB Map Generation

The MRM data were obtained from the CE-2 satellite, orbiting the Moon from October 2010 to June 2011 at an altitude of ~100 km [21,40]. The MRM instrument obtained a total of approximately 3650 observation records in one orbital period (118 min), of which 1825 observation records were obtained from south to north; the same number of observation records was obtained on the other orbit from north to south. The MRM instrument operated at 3.0 GHz, 7.8 GHz, 19.35 GHz, and 37 GHz, reflecting the microwave thermal emission features of the lunar regolith within the penetration depth, at approximately 10 to 20 times the wavelength used [34,39]. The observation angle of the instrument was 0°. The radiometric sensitivity of the MRM data was better than 0.5 K [21].

The 2C-level MRM data were used in this study and geometric correction and radiometric calibration were performed on the raw data [21,22,40]. The data were stored in PDS format, comprising the observation time, four-channel TB values, solar azimuth and incident angles, longitude, latitude, orbit elevation, and data quality. Measurements in each track were stored in a single file. Each file contains a header and a table of measured data. The header provided background data information and described the meaning of every table column.

In the B-K region, the change in TB was approximately 4 K at 3.0 GHz, 9 K at 7.8 GHz, 24 K at 19.35 GHz, and 51 K at 37 GHz in a lunation, which was much greater than that brought by the surface materials, approximately 2.9 K at 3.0 GHz, 3.5 K at 7.8 GHz, 4.2 K at 19.35 GHz, and 4.4 K at 37 GHz at noon along the latitude (sampled at 14°S). Thus, it is necessary to transcribe the MRM data points into 24 local lunar hours to comparatively enhance the TB variation with surface materials [20,21,36]. The local time of each MRM record was expressed as the relative position of the Sun with respect to the celestial sphere using the Lunar Equatorial Coordinate System (LECS) instead of the Horizon Coordinate System (HCS). The hour angle,  $h$ , can be obtained by the transforming the HCS, and the LECS is expressed as follows [20]:

$$\tan h = \sin \alpha \sin i / (\cos \alpha \cos i - \sin \varphi \cos \alpha \cos i) \quad (9)$$

where  $i$  is the solar incident angle,  $\alpha$  is the solar azimuth angle, and  $\varphi$  is the latitude, which can be read from the header of the original MRM file.

According to the calculated hour angles, the data points were divided into 24 intervals corresponding to 24 h in a lunation. The data points from 4:00 to 5:00, 6:00 to 7:00, 9:00 to 10:00, 11:00 to 12:00, 13:00 to 14:00, 17:00 to 18:00, 20:00 to 21:00, and 22:00 to 23:00 were sufficient to generate TB maps covering the whole B-K region. In this study, the data points

from 11:00 to 12:00 and from 22:00 to 23:00 (as shown in Figure 3) are used to map the B-K region at noon and night, representing two nearly extreme values over the lunar surface.

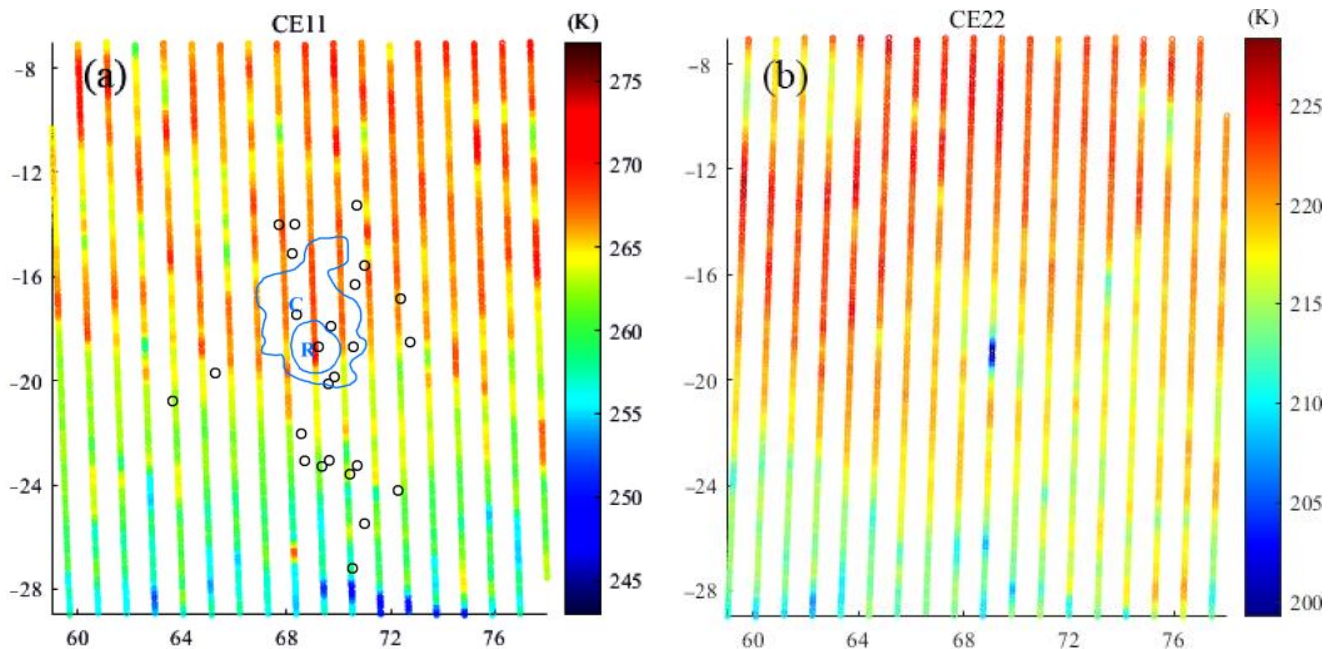


**Figure 3.** Scatter maps of the selected MRM data points in the B-K region at 37 GHz (unit: K): (a) 11:00–12:00 (noon); (b) 22:00–23:00 (night). Regions C and R within the blue lines are two special regions that are mentioned in the following sections. The DHCs identified by Hawke et al., [5] are black circles.

Figure 3 shows that the original spatial resolution of the selected MRM data points at a one-hour angle was approximately  $1^\circ$  in the direction of longitude and very high in the direction of latitude. Moreover, the change in TB along the direction of latitude was much less than that along the direction of longitude. Thus, the Delaunay triangulation linear interpolation method [41] was used to generate TB maps of the B-K region with a spatial resolution of  $0.25^\circ \times 0.25^\circ$  (Figure 4), and the data points at other hourly angles were used as references to validate the TB behaviors of the surface deposits in this study. In Figure 4c,d, the RMSE is 2.573 for daytime and 3.060 at night, indicating that the interpolated data well represent the observation data. Moreover, Cai and Lan [40] and Zheng et al., [21] provided the global TB maps using the CE-2 MRM data, which show the approximate data range in the B-K region. Further, Figure 4 shows that the TB performances in the Langrenus, Petavius, and La Pérouse craters are clearly different from their surrounding regions, illustrating the reasonableness of the TB maps in geography. Thus, the interpolated TB maps are rational.

However, one disadvantageous phenomenon should be mentioned: the change in TB in the direction of longitude was considerably large, much larger than that exhibited by the difference in the regolith components indicated by the TB values along the same latitude (Figure 4). The latitude-dependent TB variations must be weakened before applying the TB maps to understand the surface deposits in the B-K region.

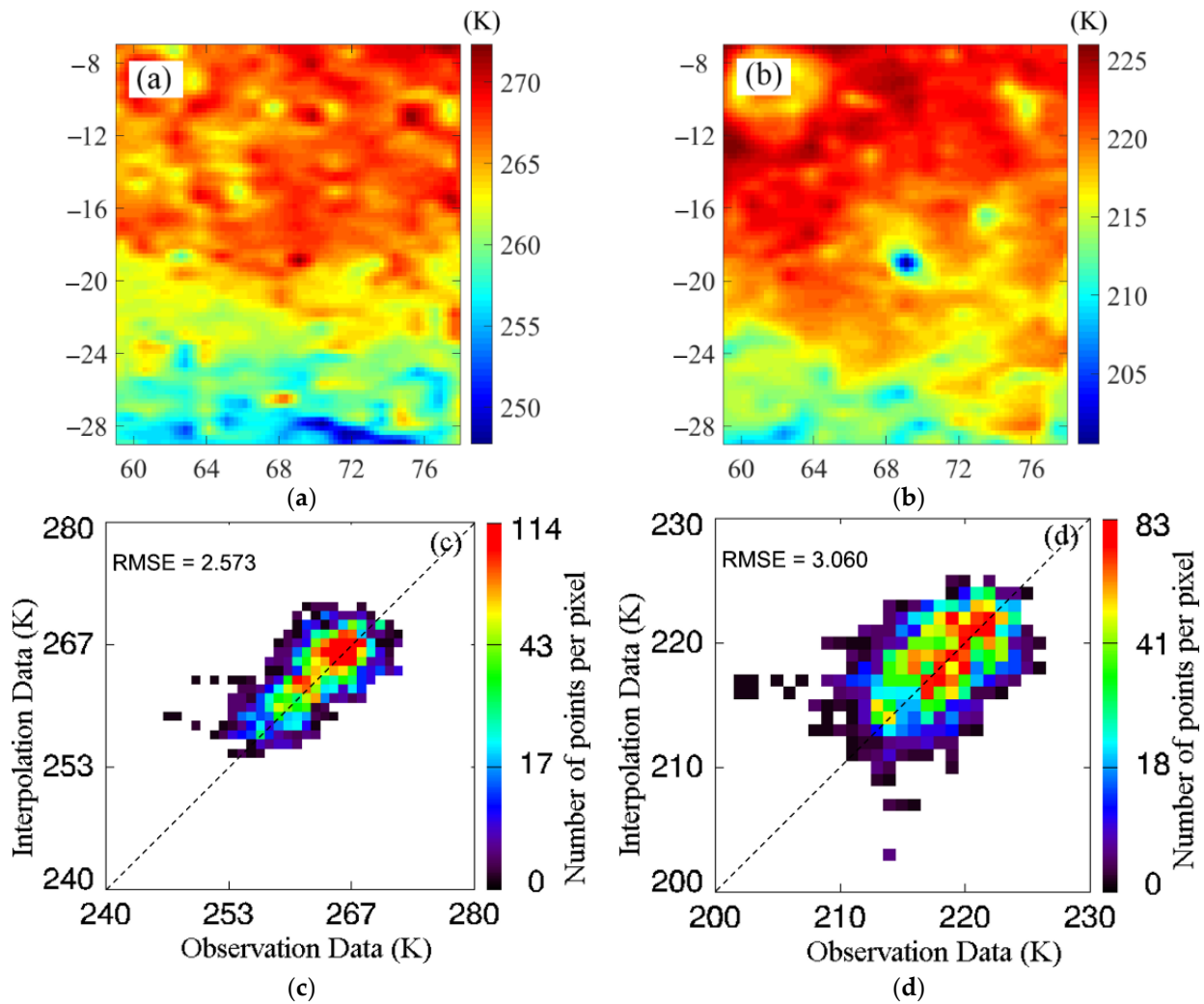


**Figure 4.** TB maps of the B-K region at 37 GHz at noon (a) and night (b), and comparisons of observation data and interpolation data at noon (c) and night (d).

### 3.3. Normalized TB (*nTB*) Maps

The normalized TB, referred to as *nTB*, was defined by Meng et al., [34], and is applied to weaken the variations of the TB in the direction of longitude [22,33,34].

To obtain the *nTB*, the standard TB (*sTB*) at each latitude was first calculated, which was expected to obtain the TB points observed under similar surface conditions. Then, the specific surface conditions, or the criteria for the selection of surface areas to calculate the *sTB*, for selecting MRM data points were designated using the following criteria:  $12\% < \text{FTA} < 15\%$ ; surface slope  $< 2^\circ$ ; and rock abundance (RA)  $< 0.005$ . The FTA, surface slope, and RA data were generated with the Clementine UV-VIS data, LRO LOLA, and Diviner data, respectively. Then, a series of sampling TB points ( $\text{TB}(\varphi_1), \dots, \text{TB}(\varphi_n)$ ) conforming to specific surface conditions were selected. Next, a degree-seven polynomial fitting scheme was adopted to describe the general variation of TB versus the latitude at each channel and each time,

$$sTB(\varphi) = a + a_1 * \varphi + a_2 * \varphi^2 + a_3 * \varphi^3 + a_4 * \varphi^4 + a_5 * \varphi^5 + a_6 * \varphi^6 + a_7 * \varphi^7 \quad (10)$$

where  $\varphi$  is the latitude, and  $a, a_1, a_2, a_3, a_4, a_5, a_6,$  and  $a_7$  are constants obtained based on the sampling MRM data points. Here, the fitted value is defined as the *sTB*( $\varphi$ ) of the

corresponding latitude  $\varphi$ . Finally, the nTB maps at noon and night can be determined by the following expression:

$$nTB(\xi, \varphi) = TB(\xi, \varphi) / sTB(\varphi) \quad (11)$$

where  $\xi$  is the longitude. Figures 5 and 6 are the generated nTB maps at noon and night, respectively. Here, the definitions of the nTB and sTB are suitable for the whole Moon surface.

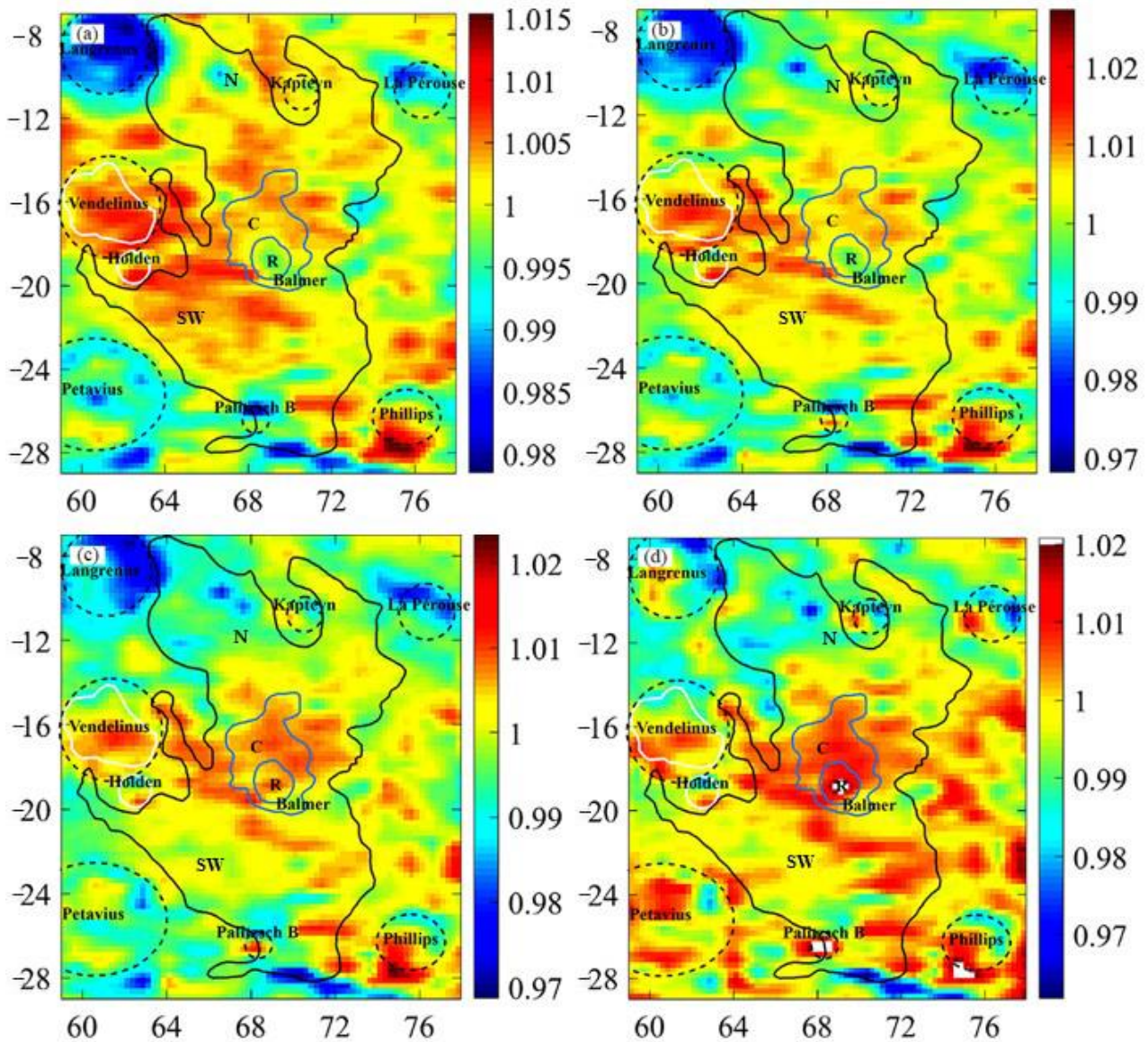


**Figure 5.** nTB maps of the B-K region at noon: (a) 3.0 GHz, (b) 7.8 GHz, (c) 19.35 GHz, (d) 37 GHz. The black line denotes the cryptomare unit and the white line denotes the mare unit interpreted by Hawke et al., [5], as shown in Figure 2b. Regions C and R within the blue lines are two special regions that are mentioned in the following sections. Region N is the northern area between the Langrenus and Kapteyn craters within the cryptomare region. Region SW is the southwestern area within the cryptomare region.

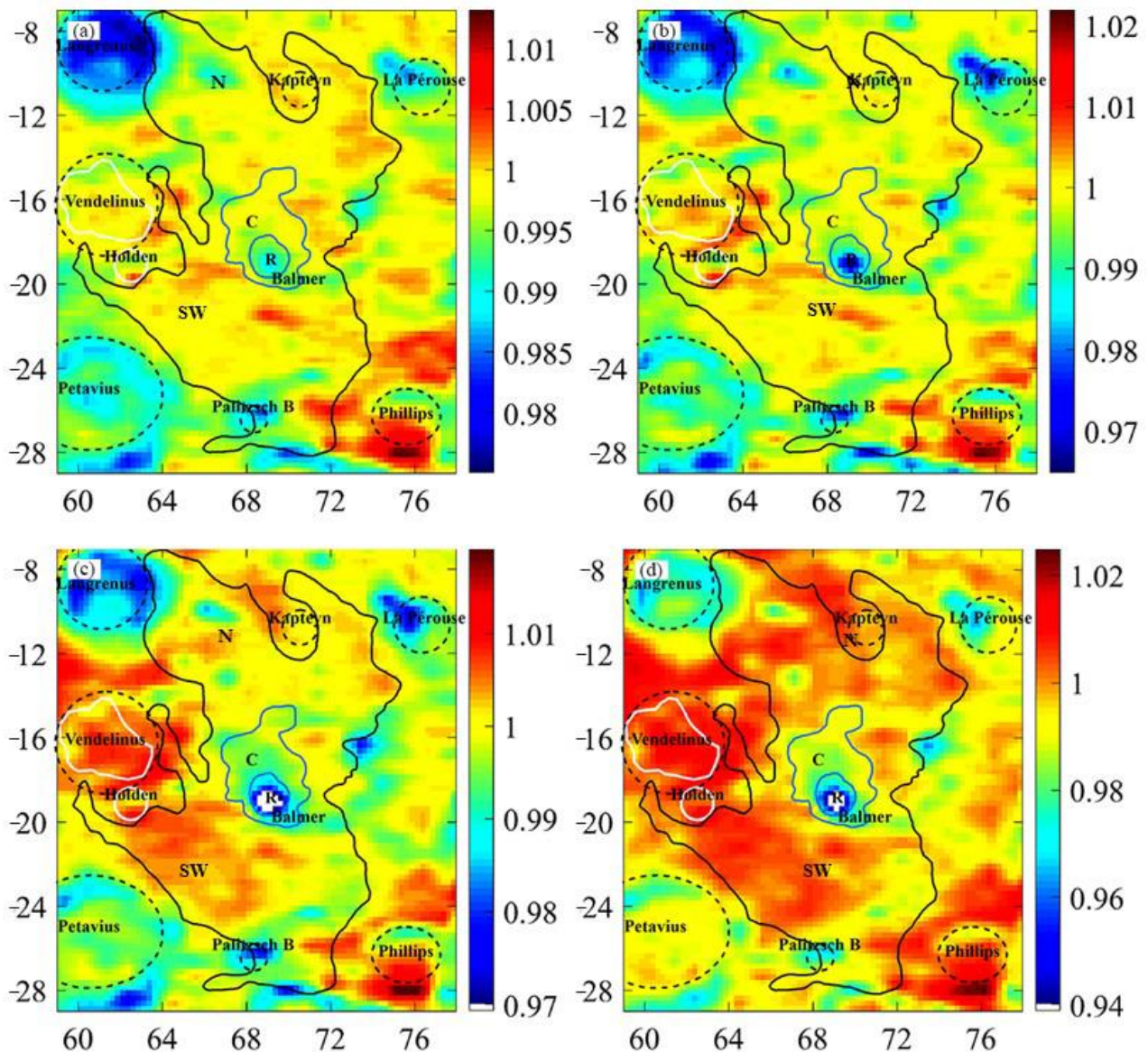


**Figure 6.** nTB maps of the B-K region at night: (a) 3.0 GHz, (b) 7.8 GHz, (c) 19.35 GHz, (d) 37 GHz. The black line denotes the cryptomare unit and the white line denotes the mare unit interpreted by Hawke et al., [5], as shown in Figure 2b. Regions C and R within the blue lines are two special regions that are mentioned in the following sections. Region N is the northern area between the Langrenus and Kapteyn craters within the cryptomare region. Region SW is the southwestern area within the cryptomare region.

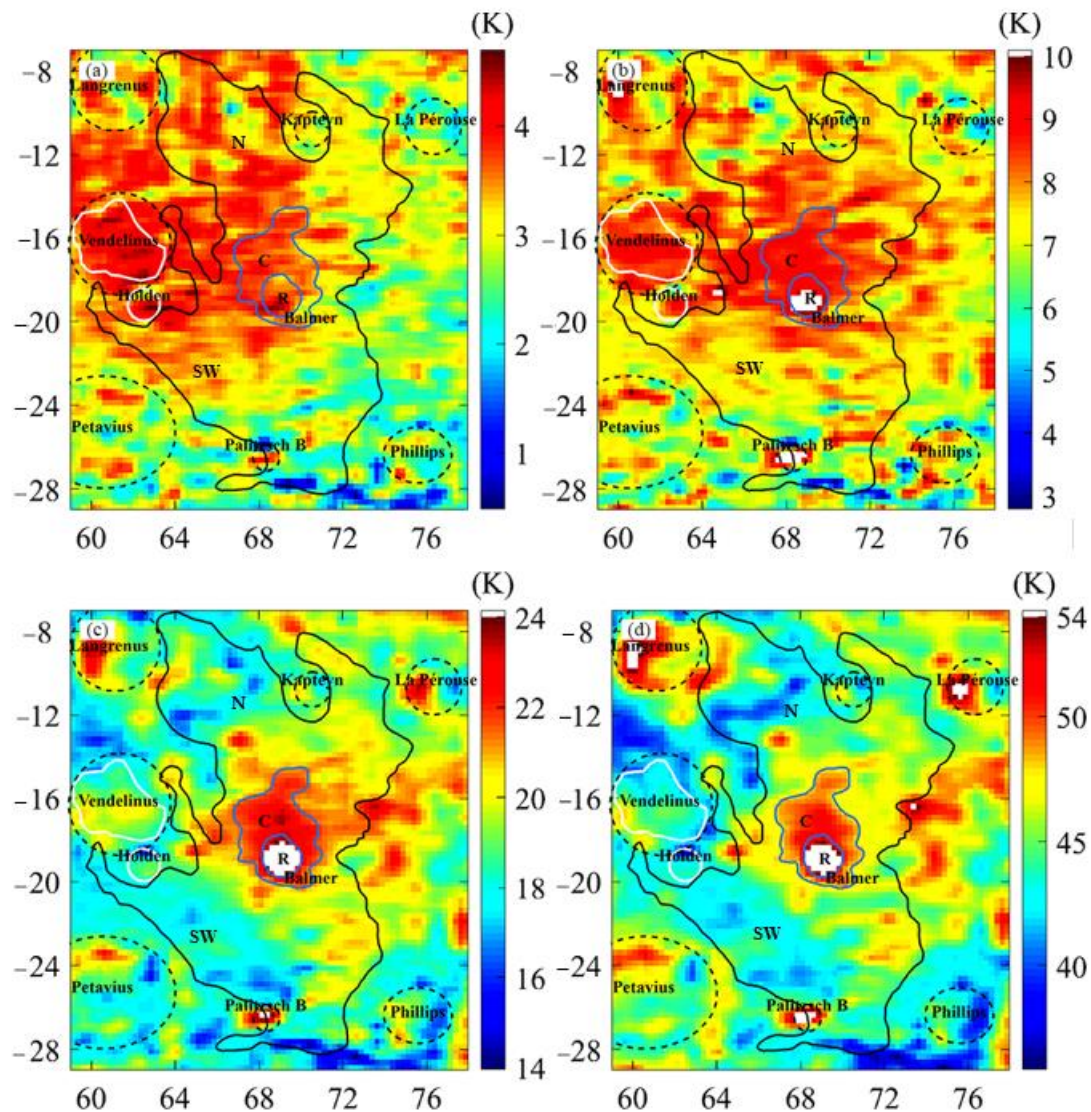
To better understand TB performances, the sketched geological map of the B-K region (Figure 2b) created by Hawke et al., [5] was vectorized and overlaid on the generated maps. Figures 5 and 6 show that the latitude-dependent effects of TB were clearly weakened compared with the TB maps in Figure 4, where the values were almost the same along the longitude except for large craters and cryptomare regions. Additionally, the correlation between the mare materials and nTB performances was relatively enhanced, which is clearly illustrated by the daytime nTB of the mare unit within green lines. Compared with the TB maps, many more regions exhibited distinct nTB performances.

Figure 4 shows that the change in the 37-GHz TB in the direction of latitude was more than 20 K both at noon and at night, which was much larger than that in the direction of longitude with similar solar illumination. In Figures 5 and 6, the change in the nTB in the

direction of latitude was weakened. Additionally, the change in the nTB in the direction of latitude was similar to that in the direction of longitude, also indicating that the variation in the nTB in the direction of latitude is effectively weakened. The nTB maps provide a different view of the surface deposits in the B-K region compared with the optical images.

### 3.4. TB Difference (dT<sub>B</sub>) Maps

The TB difference, referred to as dTB, is defined as the difference between the noon and the night TB values; it has also been shown to be sensitive to the dielectric properties of the regolith [22,34]. The dTB maps were obtained by subtracting the night TB values from the noon TB values at the same frequency (Figure 7).



**Figure 7.** dTB maps of the B-K region: (a) 3.0 GHz, (b) 7.8 GHz, (c) 19.35 GHz, (d) 37 GHz. The black line denotes the cryptomare unit and the white line denotes the mare unit interpreted by Hawke et al., [5], as shown in Figure 2b. Regions C and R within the blue lines are two special regions that are mentioned in the following sections. Region N is the northern area between the Langrenus and Kapteyn craters within the cryptomare region. Region SW is the southwestern area within the cryptomare region.

Compared with the TB maps, the latitude-dependent effect was also substantially weakened in the dTB maps, which was clearly illustrated by the values along the longitude beyond the cryptomare region. To date, MRM data have not been employed to evaluate

cryptomare deposits on the Moon. Thus, it is difficult to evaluate the reasonableness of the generated maps. Interestingly, Figure 7d shows that the dTB values were well limited within the Langrenus crater, La Pérouse crater, Palitzsch crater B, and several other craters, where the crater rims were also the boundaries of the relatively higher and lower nTB values corresponding to the enhanced and decreased solar illuminations. This suggests the appropriateness of TB values in geographical positions.

Here, two issues should be mentioned.

The first issue is the choice of observation time for generating the dTB maps. According to the definition, dTB maps can be generated with the original TB datasets at two different observation times. We generated dTB maps at the other two times and they yielded a similar description of the surface deposits, as shown in Figure 7. This again indicates that the generated TB and dTB maps were reasonable.

The second issue is the calibration problem of the MRM data. Hu et al., [42,43], Wei et al., [44], and Yang et al., [45] calibrated the data, respectively, indicating that the MRM data are rational in general. Here, we mentioned that the noontime nTB in the Langrenus, La Pérouse, Phillips, and Kapteyn craters (70.6°E, 10.8°S) was relatively higher on the western slope oriented toward solar illumination (heated in the morning) and colder on the eastern slope. Moreover, as discussed in the following sections, the TB performances in Region C were similar to those in the regions with mare deposits [34] and those in Region R were similar to those in regions with abundant rocks [33]. Thus, comparatively, the nTB and dTB maps imply for both in locating geographical positions and in representing the surface deposits and can be used to evaluate the complex cryptomare deposits in the B-K region.

Additionally, although the original spatial resolution of the selected MRM data points was approximately 1° along the latitude, the appropriateness of the nTB and dTB maps suggests that the data processing methods and the instrument calibrations have a negligible impact on reassessing the surface deposits in the B-K region using the MRM data.

#### 4. Results

Because microwave data are highly sensitive to the temperature and compositions of the regolith within the corresponding penetration depth, the MRM data provided a new view of the surface deposits in the mare units, the cryptomare units, and the highland materials referring to the geological units identified by Hawke et al., [9].

##### 4.1. Mare Unit

The mare unit is mainly distributed in the Vendelinus crater (61.5°E, 16.5°S) and the Holden crater (62.5°E, 19.2°S), which have lower reflectance and high (FeO + TiO<sub>2</sub>) abundance (FTA) values [9]. In the mare unit, Figure 5 shows a relatively high nTB at noon in the central part of Vendelinus crater, while the nTB is relatively low at 3.0 and 7.8 GHz at night, and it is similar to that in the nearby regions at 19.35 GHz and 37 GHz, as shown in Figure 6. The dTB performances of the mare unit corresponded to its nTB performances, where the values are nearly highest at 3.0 and 7.8 GHz, but they are as low as those of nearby regions at 19.35 and 37 GHz, as shown in Table 1.

**Table 1.** The average nTB and dTB values of mare unit (M) and nearby regions (NR).

| Channel   | nTB at Noon |       | nTB at Night |       | dTB     |         |
|-----------|-------------|-------|--------------|-------|---------|---------|
|           | M           | NR    | M            | NR    | M       | NR      |
| 3.0 GHz   | 1.007       | 0.996 | 0.999        | 1.001 | 4.07 K  | 3.95 K  |
| 7.8 GHz   | 1.010       | 1.007 | 1.002        | 1.004 | 8.99 K  | 8.52 K  |
| 19.35 GHz | 1.006       | 1.001 | 1.007        | 1.007 | 19.52 K | 19.49 K |
| 37 GHz    | 1.002       | 0.994 | 1.011        | 1.011 | 43.59 K | 43.45 K |

The nTB and dTB performances highlight the first problem in this study. Here, the TB performances belonged to the mare units with the highest FTA in the B-K region [9]. According to the simulation results, the TB of the FTA-rich regolith should be higher than that of the FTA-poor regolith at noon but lower at night. The nTB and dTB behaviors at 3.0 and 7.8 GHz agree with the theoretical simulation. However, the TB performances at 19.35 and 37 GHz do not coincide with the theoretical simulation. The causes of the abnormal TB performances at 19.35 and 37 GHz will be analyzed in Section 5.2.

Additionally, two issues should be mentioned.

First, the extent of the region with high daytime nTB decreases greatly in the 3.0 GHz map compared with the 37 GHz map, meaning that the dielectric properties of the regolith decrease greatly in the vertical direction compared with those with constantly high nTB values.

Second, the range indicated by the high nTB and dTB performances is much narrower than that found with the optical data by Hawke et al., [5], meaning that the dielectric properties of the regolith change greatly in the lateral direction.

The two phenomena can be explained by the fact that the B-K region experienced multiple ejecta coverings from different sources [5], implying that the surface deposits in the B-K region are rather complex.

#### 4.2. Cryptomare Unit

The cryptomare unit consists of mare deposits covered by the impact ejecta. Thus, it has no apparent visible features.

Figures 5–7 show the complex TB performances of the cryptomare deposits. Compared with the visible result with limited penetration ability and the LP-GRS result with low spatial resolution, the nTB and dTB maps show an inhomogeneous distribution of the surface deposits, because the high and low values occur irregularly in the cryptomare region, except in the central regions marked C and R, indicating the inhomogeneity of the surface deposits in the lateral direction. Comparatively, there are apparent changes in the nTB and dTB maps with frequency, except in the central regions marked C and R, indicating clear variations in the surface deposits in the vertical direction. Here, Region C was outlined based on the 48-K contour and Region R was outlined based on the 52-K contour in the 37-GHz dTB map.

In the cryptomare unit, the regular TB performances occur in the central part marked C, which indicates relatively high nTB values at noon, relatively low nTB values at night, and relatively high dTB values. Similar TB performances are also found in the basaltic deposits of the Maria Imbrium, Moscoviense, Apollo Basin, and Rümker regions (Figure 8) [22,34].

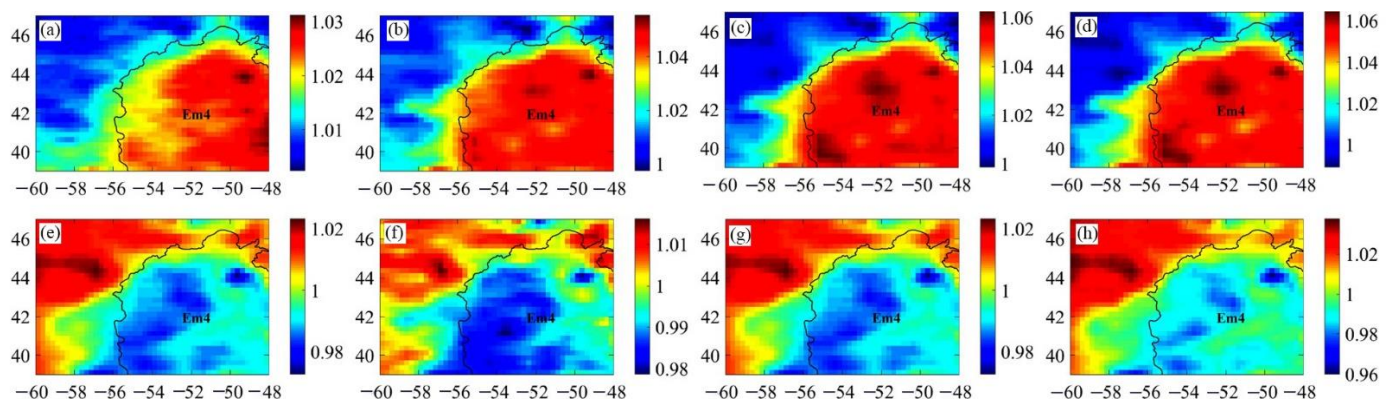


**Figure 8.** nTB maps in the Rümker region [22] at noon: (a) 3.0 GHz, (b) 7.8 GHz, (c) 19.35 GHz, (d) 37 GHz; and at night: (e) 3.0 GHz, (f) 7.8 GHz, (g) 19.35 GHz, (h) 37 GHz. The black line denotes the Em4 unit with the highest FTA.

Therefore, the material in Region C appears to be mare deposits. In other words, a mare deposit is found in the cryptomare region; the genetic mechanism and the geological meaning of which is the first topic that will be addressed in the following section.

The variation in the values in Region C is relatively small in the four channels and in the spatial domain, indicating that the deposits in Region C are homogeneous in the vertical and lateral directions. Although the TB proximate to Region C exhibits similar performances, the dTB values at 37 GHz are clearly lower than those in Region C, indicating the vertical inhomogeneity of the regolith in the surrounding area.

Referring to Region C, the TB performances are discretely different in the northern part near the Langrenus crater, in the southwestern part near the Petavius crater, and in the region marked R.

The nTB in the northern area (named Region N) between the Langrenus and Kapteyn craters is nearly the lowest at noon and relatively high at night, especially at the 19.35 and 37 GHz maps. In the dTB maps, the values are similar to those in Region C at 3.0 GHz, slightly lower than those in Region C at 7.8 GHz, and much lower than those in Region C at 19.35 and 37 GHz, as shown in Table 2.

**Table 2.** The average nTB and dTB values of Region C (C), Region R (R), northern (N), and southwestern (SW) areas within the B-K cryptomare region.

| Channel   | nTB at Noon |       |       |       | nTB at Night |       |       |       | dTB     |         |         |         |
|-----------|-------------|-------|-------|-------|--------------|-------|-------|-------|---------|---------|---------|---------|
|           | C           | N     | SW    | R     | C            | N     | SW    | R     | C       | N       | SW      | R       |
| 3.0 GHz   | 1.003       | 1.002 | 1.005 | 0.998 | 0.996        | 0.998 | 1.000 | 0.991 | 3.78 K  | 3.39 K  | 3.49 K  | 3.86 K  |
| 7.8 GHz   | 1.006       | 1.000 | 1.007 | 0.999 | 0.995        | 1.001 | 1.003 | 0.980 | 8.86 K  | 7.04 K  | 7.66 K  | 10.87 K |
| 19.35 GHz | 1.007       | 0.994 | 1.003 | 1.006 | 0.994        | 1.003 | 1.005 | 0.969 | 22.76 K | 17.83 K | 18.45 K | 28.07 K |
| 37 GHz    | 1.007       | 0.986 | 1.000 | 1.016 | 0.985        | 1.007 | 1.006 | 0.943 | 50.71 K | 41.05 K | 43.33 K | 61.57 K |

In the southwestern area (named Region SW), the nTB at noon is highest at 3.0 GHz and second highest in the other channels; at night, it is second highest at 3.0 and 7.8 GHz and highest at 19.35 and 37 GHz. The dTB performances were complex: only at 19.35 and 37 GHz does it homogeneously postulate the lowest values (Table 2).

Here, we noted that the 19.35- and 37-GHz TB performances are unique in the northern and southwestern areas and even in the mare unit, the reason for which will be further discussed in the following section.

In Region R, at daytime, the nTB is relatively low at 3.0 and 7.8 GHz, similar at 19.35 GHz, and is clearly higher at 37 GHz compared with that of the nearby regions. The nTB at night is clearly lower and the dTB is apparently higher than that in the vicinity (Table 2). Interestingly, such TB performances also are observed in the Necho, King, and Giordano Bruno craters and in the Vavilov crater (Figure 9) [33], where they are attributed to the existence of rocks because of the strong correlation between TB anomalies and high rock abundances. This hypothesis is also verified by the theoretical simulation by Meng et al., [33]. Thus, evidence suggests there are abundant rocks in Region R. If that is the case, the origin of the rocks and their geological significance should be discussed.

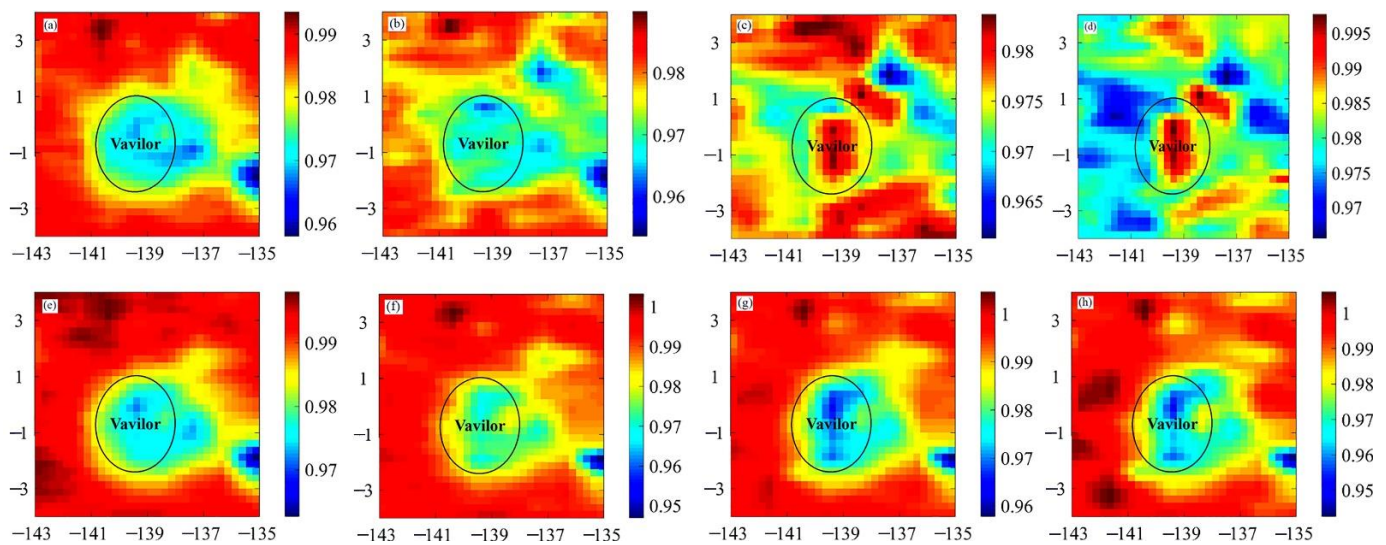


**Figure 9.** nTB maps of the Vavilor crater at noon: (a) 3.0 GHz, (b) 7.8 GHz, (c) 19.35 GHz, (d) 37 GHz; and at night: (e) 3.0 GHz, (f) 7.8 GHz, (g) 19.35 GHz, (h) 37 GHz. The black line denotes the Vavilor crater with abundant rocks identified using LRO Diviner data by Bandfield et al., [46].

The abovementioned three phenomena have not been mentioned in previous studies, indicating the unique ability of MRM data to advance our understanding of the surface materials within the cryptomare unit.

#### 4.3. Highland Materials

The highland materials are mainly distributed in the eastern part of the B-K region, mainly from 14 °S to 22 °S, excluding the impact ejecta from the La Pérouse and Phillips craters. At noon, the nTB is higher in the eastern part than in the western part, as shown in Table 3. At night, the four-channel nTB is higher in the eastern part than in the western part. However, the dTB is higher in the eastern part than in the western part (Table 3). The nTB and dTB of this kind have not been found in other regions of the Moon, which will be further studied in the future.

**Table 3.** The average nTB and dTB values of the eastern part (E) of the highland region and the western part (W) of the highland region.

| Channel   | nTB at Noon |       | nTB at Night |       | dTB     |         |
|-----------|-------------|-------|--------------|-------|---------|---------|
|           | E           | W     | E            | W     | E       | W       |
| 3.0 GHz   | 1.003       | 0.996 | 1.000        | 0.996 | 2.96 K  | 2.39 K  |
| 7.8 GHz   | 1.005       | 0.997 | 0.999        | 0.995 | 7.82 K  | 7.64 K  |
| 19.35 GHz | 1.006       | 0.997 | 0.999        | 0.995 | 20.73 K | 19.68 K |
| 37 GHz    | 1.007       | 0.995 | 0.995        | 0.989 | 47.82 K | 46.07 K |

The nTB is relatively lower in the eastern rim of the Langrenus crater, the northern and eastern rims of the La Pérouse crater, and the northern rim of the Phillips crater both at noon and at night. This TB performance is similar to that in the Tycho and Jackson craters [33], indicating the influence of the surface topography on the nTB performances. Thus, the influence of the topography should be considered in evaluating the nTB performances of the surface deposits. We also found that the aforementioned phenomena are fairly weakened in the dTB maps. In particular, the northern rim of the Phillips crater exhibited high dTB values, indicating that the influence of the surface topography on the dTB performance is limited.

Thus, the nTB maps were employed to evaluate the thermal emission features of the surface deposits, with the surface topography taken into account, and the dTB maps were employed to characterize the distribution of the surface deposits.

## 5. Discussions

### 5.1. A New View of the Surface Deposits in the B-K Region

#### 5.1.1. Mare-Like Cryptomare Deposits

In the previous analysis, we were convinced of the existence of mare deposits in Region C based on the nTB and dTB performances. However, Hawke et al., [5] and Wang and Qiu [7] both proposed that the thickness of the surface coverage by the highland materials was at least 33 m in the B-K region, which is much larger than the penetration depth of the MRM (at most 2-m penetration depth). So, how can we explain the finding regarding the mare deposits in Region C?

To answer this question, the difference between the optical and the microwave data should be noted. Compared with the optical data, which are sensitive to the color or tone of the surface, microwaves are sensitive to the dielectric features of the surface deposits at the penetration depth. In Region C, although the whole B-K region is covered by bright highland deposits, Hawke et al., [5] concluded that the cryptomare deposits surrounding the DHCs contain 30% to 53% mare materials with higher FTA. Additionally, Huang et al., [35] postulated that the distantly sourced particles delivered via ballistic transportation of ejecta from distal impact craters are important components of the lunar regolith. When ejecta land on the target surface, local materials are excavated by and mixed with the ejecta by ballistic sedimentation processes [47]. Thus, the ferrous abundance of the regolith can be enhanced in the region with buried mafic-rich deposits. This fact can also be verified by the retrieved components from the LP-GRS data in the B-K region, where a mafic-geochemical anomaly was identified with FeO abundance ranging from 7 wt.% to 11 wt.%, which was apparently higher than that in the highlands [5]. Thus, as mentioned in Section 2, the elevated mafic-rich mare materials in the surface deposits will increase the TB measured by the MRM instrument.

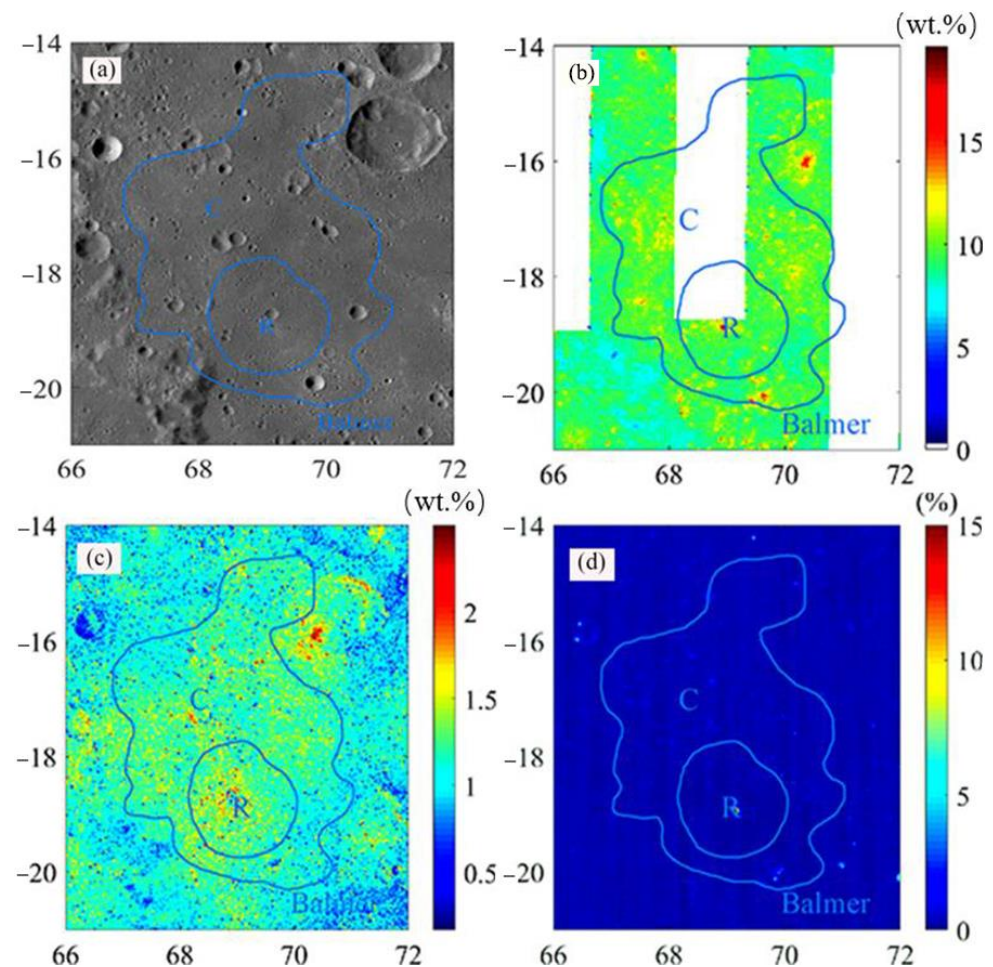
Moreover, as the key to identifying cryptomare deposits, space weathering and late impact events have a significant influence on the evolution of the DHCs. Schultz and Spudis [3] and Hawke et al., [5] noted that the albedo contrasts between dark impact materials and bright ejecta deposits decrease with time, which is disadvantageous for identifying DHCs. However, the mafic-rich nature of the materials does not change with time, which will be clearly indicated by the TB data with strong dielectric sensitivity. This is advantageous for re-evaluating the surface deposits in the cryptomare region with MRM data.

However, in the B-K cryptomare region, the existence of mare deposits is impossible, because the impact ejecta is as thick as at 33 m, as reported by Wang and Qiu [7]. Thus, we denote the materials found in Region C as mare-like cryptomare deposits (MCD). As shown in Table 4, the 3.0- and 7.8-GHz nTB at noon and dTB in Region C were lower than those in the mare unit but higher than those in the highland region. This performance agrees well with the theoretical simulation in Section 2, verifying that the MCD in Region C is a mixture of mare deposits and highland debris. This is an important finding in lunar surface research, because it is the first time that the mare-like deposits on the Moon have been directly detected and it verifies the unique ability of MRM data to further our understanding of surface deposits.

**Table 4.** The average and standard deviation nTB and dTB values of the mare unit (M), Region C (C), and highland materials (H).

| Channel   | nTB at Noon        |                    |                    | nTB at Night       |                    |                    | dTB                  |                      |                      |
|-----------|--------------------|--------------------|--------------------|--------------------|--------------------|--------------------|----------------------|----------------------|----------------------|
|           | M                  | C                  | H                  | M                  | C                  | H                  | M                    | C                    | H                    |
| 3.0 GHz   | 1.007<br>± 0.00054 | 1.003<br>± 0.00061 | 0.998<br>± 0.00098 | 0.999<br>± 0.00043 | 0.996<br>± 0.00096 | 0.998<br>± 0.00124 | 4.07 K<br>± 0.15593  | 3.78 K<br>± 0.14920  | 2.41 K<br>± 0.15643  |
| 7.8 GHz   | 1.010<br>± 0.00164 | 1.006<br>± 0.00070 | 0.999<br>± 0.00110 | 1.002<br>± 0.00110 | 0.995<br>± 0.00111 | 0.999<br>± 0.00163 | 8.99 K<br>± 0.23262  | 8.86 K<br>± 0.16569  | 6.74 K<br>± 0.21549  |
| 19.35 GHz | 1.006<br>± 0.00161 | 1.007<br>± 0.00126 | 0.996<br>± 0.00119 | 1.007<br>± 0.00094 | 0.994<br>± 0.00104 | 1.000<br>± 0.00111 | 19.52 K<br>± 0.39395 | 22.76 K<br>± 0.35832 | 18.19 K<br>± 0.28697 |
| 37 GHz    | 1.002<br>± 0.00243 | 1.007<br>± 0.00138 | 0.993<br>± 0.00172 | 1.011<br>± 0.00210 | 0.985<br>± 0.00210 | 1.000<br>± 0.00145 | 43.59 K<br>± 0.84514 | 50.71 K<br>± 0.59108 | 43.06 K<br>± 0.60858 |

The WAC image (Figure 10a) shows that the tone is slightly darker and the density of the craters is lower within Region C than in the surrounding area. The FeO abundance (FA) map indicates a continuous distribution and relatively high FA in Region C (Figure 10b), where the average FA is 10.4 wt.% and is 0.3 wt.% higher than that of surrounding areas. Figure 10c shows a similar TiO<sub>2</sub> distribution as the FA map in Region C, where the TiO<sub>2</sub> abundance (TA) is only 0.16 wt.% higher than that in its vicinity. Thus, the existence of MCD in Region C is supported by the data.

**Figure 10.** The special region in the B-K region: (a) WAC image, (b) FeO abundance map, (c) TiO<sub>2</sub> abundance map, (d) rock abundance map.

Moreover, Figure 10d indicates that the rock abundance (RA) is largely similar within and surrounding Region C, indicating that the existence of MCD is not related to the surface rocks. Additionally, the MCD is not identified by the optical and thermal infrared data in previous studies, probably because the difference in the FA, TA, and RA in Region C is rather slight compared with those of the surrounding areas.

The discovery of MCD is helpful for improving our understanding of basaltic volcanism in the B-K region. Assuming that the surface bombardments are saturated in the B-K region, two hypotheses are proposed to understand the existence of MCD in Region C.

First, the thickness of the surface ejecta above the buried mare deposits is probably thinner in Region C than in other places. If so, under the condition of similar surface bombardments, the hidden mare deposits will be excavated more in Region C with shallow surface ejecta than those with thicker surface ejecta, resulting in the higher mixture fraction of mare deposits in the highland debris.

This hypothesis is logical, because Region C is located at the intersection between the four large craters: Langrenus, La Pérouse, Phillips, and Petavius. That is, Region C is at the greatest distance from the above four craters compared with the other areas, meaning that the ejecta from the four craters should be the least abundant in the B-K region according to the cratering mechanism [48].

The problem with the hypothesis is that the surface ejecta are mainly brought by the impact ejecta forming the basins, including Serenitatis and Smythii [6], and little is known about the spatial distribution of this kind of ejecta thickness.

Second, the FTA of the buried mare deposits is likely higher in Region C than in other regions if the buried mare deposits are excavated with a similar fraction. Figure 3a shows that the distribution of the DHCs within Region C was similar to that in the nearby regions, indicating that the excavated fractions of the buried deposits should be evenly distributed. Thus, only on the condition that the buried mare deposits within Region C have a higher FTA will the surface deposits be more mafic than the nearby regions, indicating that this hypothesis should be reasonable. The remaining uncertainty for the hypothesis is that the saturated bombardments and the space weathering heavily altered the surface features, making the finding difficult to verify by the visible data.

Furthermore, no matter which hypothesis is favored, the existence of MCD provides several important clues to advance our understanding of the buried mare deposits in Region C.

Hawke et al., [5] and Wang and Qiu [7] reported that the buried mare deposits in the B-K region are rich in thorium (Th) and high in aluminum, indicating the old age of the buried deposits. However, the Th element is mainly distributed in the northern part of the B-K region near the Langrenus crater, where the MCD is located in Region C near the Balmer Basin in the southern part.

That is, if the buried mare deposits in Region C are the same as those in the northern part, the Th abundance should be much higher in Region C than in the northern part because of the existence of the identified MCD. However, the Th abundance was not enhanced in Region C in the Th map provided by Hawke et al., [5] and Wang and Qiu [7]. Thus, the buried mare deposits in Region C were lacking in the Th element, indicating that the buried mare deposits in this region are in a younger episode compared with the northern part of the B-K region.

Thus, there are at least two kinds of buried mare deposits in the B-K region, which erupted during different episodes. A similar conclusion was also proposed by Wang and Qiu [7] using the  $M^3$  data, which suggested that the younger buried mare basalt occurred in a fresh crater at (69.1°E, 18.9°S, 1.4 km) (Figure 11a, marked S, white circle) just south of Region C.

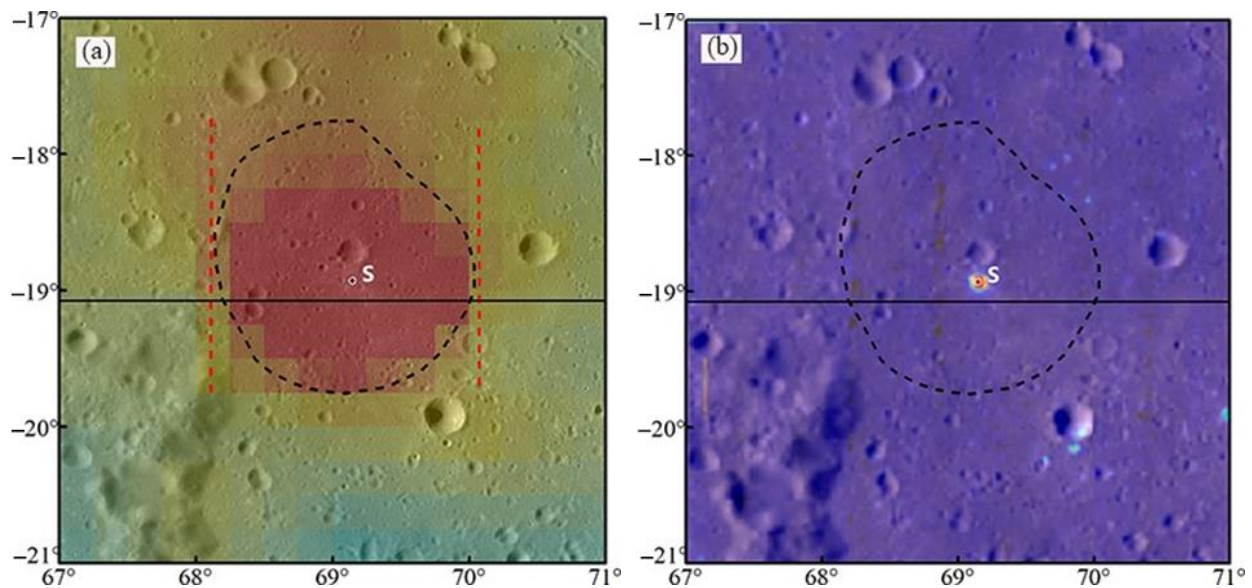


**Figure 11.** (a) The 37-GHz dTB map with 70% transparency overlaying the WAC image. (b) Diviner RA map with 70% transparency overlaying the WAC image. Mark S is the fresh crater centered at (69.1°E, 18.9°S). The black dotted line is Region R. The black profile is selected 3.9 km south of crater S with high RA values. The red dotted line is the TB anomaly in Region R.

Compared with the results by Wang and Qiu [7], who arrived at the conclusion only pointing to Crater S, the MRM data suggest a more extensive range of late-episode mare deposits. Furthermore, Figures 5–7 show that Region C is the most conservative estimation of the range with the MCD, which can be extended considerably towards the north.

### 5.1.2. A Construct-like Volcanic Feature

In the previous section, we mentioned that the TB performances in Region R were abnormal and we ascribed the differences to the presence of rocks. To better understand the formation mechanism of the TB anomaly in Region R, the 37-GHz dTB map of the anomaly was overlaid on the WAC image (Figure 11a).

Figure 11b shows that the rock abundance generated by Bandfield et al., [46] does not support the finding, because the high RA occurs only in crater S and its close vicinity within a region approximately 2.5 km in diameter, while region R is much more extensive, approximately 60 km in diameter and circular in shape. Thus, the correlation between the high RA anomaly and the formation of the TB anomaly requires further study.

Figure 11a shows that although abundant craters with diameters ranging from 1 km to 6 km occurred, no large craters or terrain could be directly responsible for the dTB anomaly in Region R. Moreover, Fa and Jin [49], Fa and Wieczorek [50], and Fang and Fa [36] proposed that the FA, TA, RA, and slope-related elevation (DEM) are important factors impacting the TB of the regolith. Thus, the aforementioned parameters in Region R are profiled in Figure 12, where the profile is selected 3.9 km south of Crater S with high RA values. Figure 12 shows that dTB is clearly elevated in Region C within the dashed lines, but FA, TA, and RA do not present correspondingly high values. Additionally, the DEM profile shows a flat surface with slight fluctuation, which also does not support the high dTB anomaly in Region R.

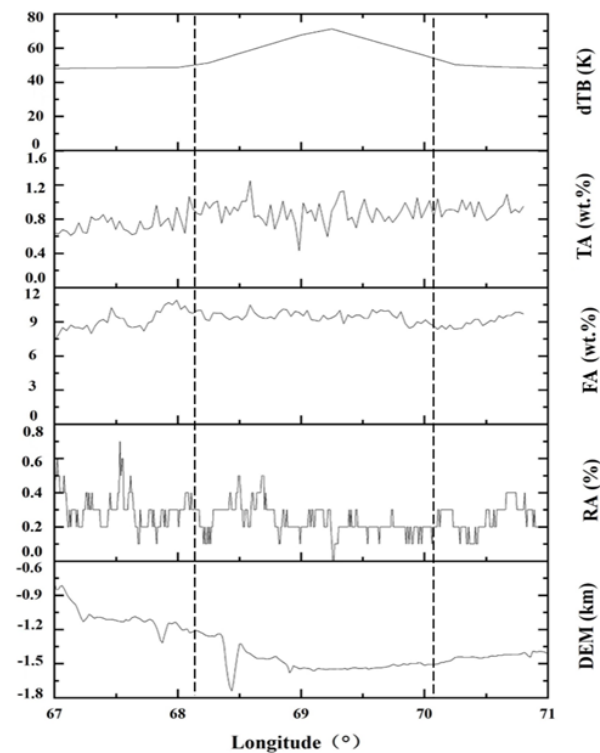


**Figure 12.** The dTB, TiO<sub>2</sub> abundance (TA), FeO abundance (FA), rock abundance (RA), and surface elevation (DEM) values along the black profile are shown in Figure 11a. The black dotted line is the TB anomaly in Region R.

As mentioned in the previous section, the TB performances suggested that abundant rocks exist in Region R, although this finding is not supported by the Diviner results. Considering that the penetration depth of the MRM microwave is at least several tens of centimeters and is much larger than the micrometer-scale penetration depth of the RA-related thermal infrared data, this phenomenon implies that there likely exists a hidden construct in Region R.

Based on Clementine UV–VIS data and M<sup>3</sup> spectra data, Hawke et al., [5] and Wang and Qiu [7] both mentioned the special compositions in crater S, which is largely in the center of the construct in region R. Wang and Qiu [7] and Qiu et al. [51] suggested that the special compositions in crater S are gabbro and monzogabbro enriched in high-Ca pyroxene. Therefore, they hypothesized that the deposits here probably represent one episode of mare volcanism or at least an intrusion of basaltic lava. Considering that Region R is located just within Region C and that they both represent late-episode volcanic activity, we propose that the hidden construct in Region R is probably a construct-like volcanic feature.

Furthermore, we mentioned that the 37-GHz dTB values gradually decrease from Region R to surrounding places in Region C in an irregular shape. Moreover, the 3.0- and 7.8-GHz nTB maps at daytime and the nighttime TB map show that Region C is apparently elongated along the northwest direction. Therefore, the existence of the construct-like volcanic feature is not brought by the interpolation process. Combined with the findings by Wang and Qiu [7] and Qiu et al., [51], these results may represent at least one potential volcanic edifice extruding the mare deposits buried in the B-K region. This also means that the MRM data have the potential to detect possible volcanic edifices, which have seldom been reported in studies of lunar volcanism and warrant further study with more sources of data.

Additionally, the influence of the substrate temperature in understanding the TB anomaly in Region R should be considered. Meng et al., [34] ascribed the relatively higher noon and night TB at 3.0 GHz on the Orientale floor to the high substrate temperature. Here, the rock-related TB performances have been fully studied with the theoretical model

in the work by Meng et al., [33]. Thus, the influence of the substrate temperature is not addressed in this study.

### 5.2. Discovering Special Materials with Strong Heat-Storage Capacity

As mentioned in Section 4.2, the 19.35- and 37-GHz TB performances were unique in the northern and southwestern parts of the cryptomare region and even in the mare unit. In the northern and southwestern parts, the dTB was similar at 3.0 GHz, slightly lower at 7.8 GHz, but obviously lower at 19.35 and 37 GHz compared with that of Region C with the MCD. Here, we termed the abnormal phenomenon in the northern and southwestern parts of the cryptomare region and in the mare unit within the Vendelinus crater as the low-dTB anomaly because it caused a considerably low dTB at 19.35 and 37 GHz. The boundary of the low-dTB anomaly is outlined in Figure 13a, which is based on the dTB performances at 37 GHz.

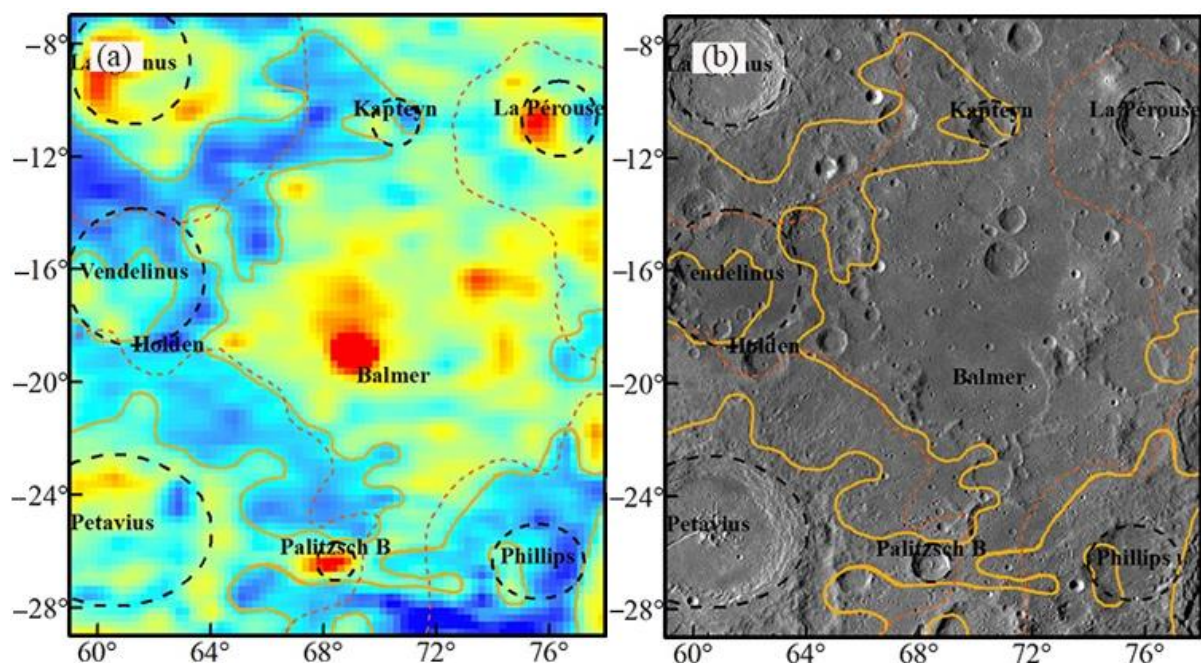


**Figure 13.** (a) Low-dTB anomaly outlined (orange line) in the dTB map at 37 GHz. (b) Boundary of the low-dTB anomaly expressed in the WAC image. The dashed lines are boundaries of the impact ejecta identified by Hawke et al., [5].

The existence of the low-dTB anomaly is reasonable and can be verified by the dTB performances in the mare unit within the Vendelinus crater. Here, the dTB should be much higher than the MCD at four channels according to the theoretical simulation. Actually, the dTB in the low-dTB anomaly was as expected only at 3.0 and 7.8 GHz, but it was abnormally lower than that of the MCD at 19.35 GHz and 37 GHz, verifying that the existence of the low-dTB anomaly is reasonable.

The regional geochemistry and chemical components of the B-K region have been fully studied by Hawke et al., [5] and Wang and Qiu [7], but none of the components appear to be responsible for the low-dTB anomaly, at least in geographical position. That is, there probably exists a new chemical component that has not been identified, at least in the B-K region, which causes the low-dTB anomaly.

Moreover, Figure 5 to Figure 7 show that the 19.35- and 37-GHz nTB in the low-dTB anomaly was considerably high at night but clearly low at noon. Thus, the special material should have a fairly strong heat-storage capacity based on the physical principles [52].

Furthermore, Figure 7 indicates that the low-dTB anomaly apparently occurred at 19.35 and 37 GHz. Thus, the thickness of the special material should be larger than 31 cm but no more than 76.9 cm, which are the penetration depths of 19.35- and 7.8-GHz microwaves

(note: Campbell et al., [39] proposed that the penetration depth of the microwave is approximately 10 to 20 times the wavelength used; here, 20 times the wavelength was assumed considering the low FeO and TiO<sub>2</sub> abundances of the surface deposits in the region).

When projecting the boundary of the low-dTB anomaly and the boundaries of the ejecta interpreted by Hawke et al., [5] on the WAC images in Figure 13b, a strong correlation between the low-dTB anomaly and the impact ejecta identified by Hawke et al., [5] was observed. We mentioned that the low-dTB anomaly in the western part comprises large portions of the ejecta from the Langrenus and Petavius craters. In the southeastern area, the special material mainly exists in the ejecta from the Humboldt crater. In particular, the boundary of the low-dTB anomaly largely agrees with the northeastern margin of the ejecta from the Petavius crater in the southwestern area. These agreements suggest that the special material is probably the ejecta of large craters. Considering the large excavation depth of large craters such as Langrenus, Petavius, and Humboldt, according to the cratering numerical simulation [48], the special material should originate in the deep layer of the lunar crust.

Furthermore, regions with such low-dTB anomalies have also been discovered in mare Moscoviense, mare Smythii, the Apollo basin, and the Copernicus crater [22,23], which suggests that special material is widely distributed over the lunar surface. Combined with the findings in this study, this provides new evidence of the heterogeneity of the lunar crust in the vertical direction.

Finally, two issues should be emphasized. First, we do not deny the existence of the cryptomare deposits identified by Hawke et al., [5] in regions with low dTB anomalies. Second, a special material with strong heat-storage capacity only occurred in the shallow layer of the regolith and the thickness is no more than 76.9 cm.

Moreover, the surface deposits beyond Regions C and R and the low-dTB anomaly were not discussed because the nTB and dTB performances are rather complex. More work should be done to assess the chemical compositions and geophysical features of the special material.

## 6. Conclusions

In this study, the cryptomare deposits in the Balmer-Kapteyn region were evaluated with the nTB and dTB maps derived with the CE-2 MRM data. Combined with the datasets including LRO WAC, LOLA, and Diviner data and Clementine UV-VIS data, the microwave thermal emission features of the cryptomare deposits in the B-K region were analyzed. The main results are summarized as follows.

The nTB and dTB performances indicate the existence of mare-like cryptomare deposits in Region C, where the tone was slightly darker and the FeO and TiO<sub>2</sub> abundances were slightly higher than those in the surrounding regions. Combined with the surface compositions, at least two kinds of buried mare deposits were indicated in the B-K region, which erupted during different episodes.

A construct-like volcanic feature was discovered in Region R according to the nTB and dTB performances; this finding is supported by the chemical components discovered by Wang and Qiu [7].

A special material that can cause the low dTB anomaly was detected in the shallow layer of the regolith, which exists in the northern and southwestern parts of the cryptomare region and in the mare unit within the Vendelinus crater. The thickness of the special material was larger than 31 cm but no greater than 76.9 cm. The special material exhibited a strong heat-storage capacity and it probably originated from the deep layer of the lunar crust, illustrating the heterogeneity of the lunar crust.

Generally, this study suggests that the CE-2 MRM data can be used to identify the surface deposits in the cryptomare region. It could complement the previous optical study and provide new insight into the surface deposits based on the regolith dielectric properties, which is impactful as a useful supplement to improve the geological mapping of the Moon.

In the future, more work is required to advance our understanding of the construct-like volcanic feature and the special material causing the low-dTB anomaly.

**Author Contributions:** Conceptualization, Z.M. and T.T.; methodology, Z.M. and Y.L.; software, Y.L.; validation, Y.Z., Z.X. and J.P.; formal analysis, Z.M., Y.Z., J.P. and X.Z.; data curation, T.T.; writing—original draft preparation, T.T. and Z.M.; writing—review and editing, T.T., Z.M., J.P., Z.X., Z.C. and X.Z.; visualization, T.T., X.D. and Y.L.; supervision, Z.X. and Y.Z.; project administration, Z.M.; funding acquisition, Z.M. All authors have read and agreed to the published version of the manuscript.

**Funding:** This research was funded by Natural Science Foundation of Jilin Province (No. 20220101159JC), the National Key R&D Program of China (No. 2021YFA0715104), the National Natural Science Foundation of China (No. 42071309), the Strategic Priority Research Program of Chinese Academy of Sciences (No. XDB 41000000), the opening fund of State Key Laboratory of Lunar and Planetary Sciences (Macau University of Science and Technology), Macau FDCT grant number 119/2017/A3, and the Science and Technology Development Fund (FDCT) of Macau (grant Nos. 0059/2020/A2, and 0042/2018/A2).

**Data Availability Statement:** In this study, the wide angle camera data used in Figures 2a, 10a, 11 and 13b are downloaded from ([https://astrogeology.usgs.gov/search/map/Moon/LRO/LROC\\_WAC/Lunar\\_LRO\\_LROC-WAC\\_Mosaic\\_global\\_100m\\_June2013](https://astrogeology.usgs.gov/search/map/Moon/LRO/LROC_WAC/Lunar_LRO_LROC-WAC_Mosaic_global_100m_June2013) (accessed on 5 March 2021)). The original TB data in Figures 3 and 4 and the processed normalized TB and TB difference data in Figures 5–9, 11a and 13a are available online (<https://doi.org/10.5281/zenodo.5540256> (accessed on 18 December 2020)), and the used CE-2 MRM data are available from Data Release and Information Service System of China's Lunar Exploration Program ([https://moon.bao.ac.cn/ce5web/searchOrder\\_pdsData.search](https://moon.bao.ac.cn/ce5web/searchOrder_pdsData.search) (accessed on 16 September 2020)) (the downloaded procedure is provided in the attachment). FeO and TiO<sub>2</sub> abundances data in Figures 10b,c, and 12 are derived with the improved Lucey model [18] using the Clementine UV-VIS data, which are downloaded online ([https://astrogeology.usgs.gov/search/map/Moon/Clementine/UVVIS/Lunar\\_Clementine\\_UVVIS\\_WarpMosaic\\_5Bands\\_200m](https://astrogeology.usgs.gov/search/map/Moon/Clementine/UVVIS/Lunar_Clementine_UVVIS_WarpMosaic_5Bands_200m) (accessed on 9 February 2022)). The surface elevation data in Figure 12 are downloaded from ([https://pds-geosciences.wustl.edu/lro/lro-l-lola-3-rdr-v1/lrolo1\\_1xxx/data/sldem2015/global/jp2](https://pds-geosciences.wustl.edu/lro/lro-l-lola-3-rdr-v1/lrolo1_1xxx/data/sldem2015/global/jp2) (accessed on 6 June 2021)), File sldem 2015 128 60s\_60n\_000\_360.jp2). The rock abundance data in Figures 10d, 11b and 12 are downloaded from [https://pds-geosciences.wustl.edu/lro/lro-l-dlre-4-rdr-v1/lroldr\\_1001/data/gdr\\_l3/cylindrical/jp2/](https://pds-geosciences.wustl.edu/lro/lro-l-dlre-4-rdr-v1/lroldr_1001/data/gdr_l3/cylindrical/jp2/) (accessed on 3 October 2021) (File dgdr\_ra\_avg\_cyl\_128\_jp2.jp2).

**Acknowledgments:** The authors express their thanks to the people helping with this work, the providers of the data used in this article, and acknowledge the valuable suggestions from the peer reviewers.

**Conflicts of Interest:** The authors declare no conflict of interest regarding the publication of this paper.

## References

1. Head, J.W.; Wilson, L. Lunar mare volcanism: Stratigraphy, eruption conditions, and the evolution of secondary crusts. *Geochim. Et Cosmochim. Acta* **1992**, *56*, 2155–2175. [[CrossRef](#)]
2. Antonenko, I.; Head, J.W.; Mustard, J.F.; Ray Hawke, B. Criteria for the detection of lunar cryptomaria. *Earth Moon Planets* **1995**, *69*, 141–172.
3. Schultz, P.H.; Spudis, P.D. Evidence for ancient mare volcanism. *Lunar Planet. Sci. Conf. Proc.* **1979**, *3*, 2899–2918.
4. Hawke, B.R.; Bell, J.F. Spectral Reflectance Studies of Dark-Haloed Impact Craters: Implications for the Composition and Distribution of Ancient Lunar Basalts. In Proceedings of the Lunar and Planetary Science Conference, University of Hawaii, School of Earth and Ocean Sciences, Manoa, HI, USA, 1 March 1983; pp. 287–288.
5. Hawke, B.R.; Gillis, J.J.; Giguere, T.A.; Blewett, D.T.; Lawrence, D.J.; Lucey, P.G.; Smith, G.A.; Spudis, P.D.; Taylor, G.J. Remote sensing and geologic studies of the Balmer-Kapteyn region of the Moon. *J. Geophys. Res. Planets* **2005**, *110*, E6. [[CrossRef](#)]
6. Whitten, J.L.; Head, J.W. Lunar cryptomaria: Physical characteristics, distribution, and implications for ancient volcanism. *Icarus* **2015**, *247*, 150–171. [[CrossRef](#)]
7. Wang, X.; Qiu, D. Lunar Cryptomare: New Insights Into the Balmer-Kapteyn Region. *J. Geophys. Res. Planets* **2018**, *123*, 3238–3255. [[CrossRef](#)]
8. Antonenko, I. Global Estimates of Cryptomare Deposits: Implications for Lunar Volcanism. In Proceedings of the 30th Annual Lunar and Planetary Science Conference, Houston, TX, USA, 15–19 March 1999; p. 1703.

9. Campbell, B.A.; Hawke, B.R. Radar mapping of lunar cryptomaria east of Orientale basin. *J. Geophys. Res. Planets* **2005**, *110*. [[CrossRef](#)]
10. Antonenko, I.; Head, J. Cryptomaria in the Schiller-Schickard, Mare Humorum and Western Oceanus Procellarum Areas: Studies Using Dark-Halo Craters. *Lunar Planet. Sci. Conf.* **1994**, *25*, 35.
11. Kaydash, V.; Shkuratov, Y.; Videen, G. Dark halos and rays of young lunar craters: A new insight into interpretation. *Icarus* **2014**, *231*, 22–33. [[CrossRef](#)]
12. Lucey, P.G.; Blewett, D.T.; Taylor, G.J.; Hawke, B.R. Imaging of lunar surface maturity. *J. Geophys. Res. Planets* **2000**, *105*, 20377–20386. [[CrossRef](#)]
13. Hawke, B.R.; Spudis, P.D. Geochemical anomalies on the eastern limb and farside of the moon. In Proceedings of the Lunar Highlands Crust, Houston, Tex., USA, 1 January 1980; pp. 467–481.
14. Hawke, B.R.; Spudis, P.D.; Clark, P.E. The origin of selected lunar geochemical anomalies Implications for early volcanism and the formation of light plains. *Earth Moon Planets* **1985**, *32*, 257–273. [[CrossRef](#)]
15. Davis, P.A., Jr. Iron and titanium distribution on the moon from orbital gamma ray spectrometry with implications for crustal evolutionary models. *J. Geophys. Res. Solid Earth* **1980**, *85*, 3209–3224. [[CrossRef](#)]
16. Lawrence, D.J.; Feldman, W.C.; Elphic, R.C.; Little, R.C.; Prettyman, T.H.; Maurice, S.; Lucey, P.G.; Binder, A.B. Iron abundances on the lunar surface as measured by the Lunar Prospector gamma-ray and neutron spectrometers. *J. Geophys. Res. Planets* **2002**, *107*, 13-1–13-26. [[CrossRef](#)]
17. Head, J.W.; Murchie, S.; Mustard, J.F.; Pieters, C.M.; Neukum, G.; McEwen, A.; Greeley, R.; Nagel, E.; Belton, M.J.S. Lunar impact basins: New data for the western limb and far side (Orientale and South Pole-Aitken Basins) from the first Galileo flyby. *J. Geophys. Res. Planets* **1993**, *98*, 17149–17181. [[CrossRef](#)]
18. Giguere, T.A.; Hawke, B.R.; Blewett, D.T.; Bussey, D.B.J.; Lucey, P.G.; Smith, G.A.; Spudis, P.D.; Taylor, G.J. Remote sensing studies of the Lomonosov-Fleming region of the Moon. *J. Geophys. Res. Planets* **2003**, *108*. [[CrossRef](#)]
19. Sori, M.M.; Zuber, M.T.; Head, J.W.; Kiefer, W.S. Gravitational search for cryptovolcanism on the Moon: Evidence for large volumes of early igneous activity. *Icarus* **2016**, *273*, 284–295. [[CrossRef](#)]
20. Zheng, Y.C.; Tsang, K.T.; Chan, K.L.; Zou, Y.L.; Zhang, F.; Ouyang, Z.Y. First microwave map of the Moon with Chang'E-1 data: The role of local time in global imaging. *Icarus* **2012**, *219*, 194–210. [[CrossRef](#)]
21. Zheng, Y.; Chan, K.L.; Tsang, K.T.; Zhu, Y.; Hu, G.P.; Blewett, D.T.; Neish, C. Analysis of Chang'E-2 brightness temperature data and production of high spatial resolution microwave maps of the Moon. *Icarus* **2019**, *319*, 627–644.
22. Meng, Z.; Lei, J.; Qian, Y.; Xiao, L.; Head, J.W.; Chen, S.; Cheng, W.; Shi, J.; Ping, J.; Kang, Z. Thermophysical Features of the Rümker Region in Northern Oceanus Procellarum: Insights from CE-2 CELMS Data. *Remote Sens.* **2020**, *12*, 3272. [[CrossRef](#)]
23. Liu, C.; Mei, L.; Meng, Z.; Wang, Y.; Zhu, K.; Cheng, W.; Cai, Z.; Ping, J.; Gusev, A. Special Thermophysical Features of Floor Materials in Mare Smythii Indicated by CE-2 CELMS Data. *IEEE J. Sel. Top. Appl. Earth Obs. Remote Sens.* **2021**, *14*, 8135–8143. [[CrossRef](#)]
24. Siegler, M.A.; Feng, J.; Lucey, P.G.; Ghent, R.R.; Hayne, P.O.; White, M.N. Lunar Titanium and Frequency-Dependent Microwave Loss Tangent as Constrained by the Chang'E-2 MRM and LRO Diviner Lunar Radiometers. *J. Geophys. Res. Planets* **2020**, *125*, e2020JE006405. [[CrossRef](#)]
25. Feng, J.; Siegler, M.A.; Hayne, P.O. New Constraints on Thermal and Dielectric Properties of Lunar Regolith from LRO Diviner and CE-2 Microwave Radiometer. *J. Geophys. Res. Planets* **2020**, *125*, e2019JE006130. [[CrossRef](#)]
26. Heiken, G.; Vaniman, D.; French, B.M. *Lunar Sourcebook—A User's Guide to the Moon*; Cambridge University Press: Cambridge, UK, 1991; 753p.
27. Keihm, S.J.; Langseth, M.G. Lunar microwave brightness temperature observations reevaluated in the light of Apollo program findings. *Icarus* **1975**, *24*, 211–230. [[CrossRef](#)]
28. Wang, Z.; Li, Y.; Jiang, J.; Li, D. Lunar surface dielectric constant, regolith thickness, and <sup>3</sup>He abundance distributions retrieved from the microwave brightness temperatures of CE-1 Lunar Microwave Sounder. *Sci. China Earth Sci.* **2010**, *53*, 1365–1378. [[CrossRef](#)]
29. Liu, N.; Jin, Y.Q. A Radiative Transfer Model for MW Cold and IR Hot Spots of Chang'e and Diviner Observations. *IEEE Trans. Geosci. Remote Sens.* **2019**, *57*, 8184–8190. [[CrossRef](#)]
30. Meng, Z.; Chen, S.; Osei, E.M.; Wang, Z.; Cui, T. Research on water ice content in Cabeus crater using the data from the microwave radiometer onboard Chang'e-1 satellite. *Sci. China Phys. Mech. Astron.* **2010**, *53*, 2172–2178. [[CrossRef](#)]
31. Berryman, J.G. Mixture Theories for Rock Properties. In *Rock Physics & Phase Relations*; American Geophysical Union Press: Washington DC, USA, 1995; pp. 205–228.
32. Hu, G.P.; Chan, K.L.; Zheng, Y.C.; Xu, A.A. A Rock Model for the Cold and Hot Spots in the Chang'E Microwave Brightness Temperature Map. *IEEE Trans. Geosci. Remote Sens.* **2018**, *56*, 5471–5480. [[CrossRef](#)]
33. Meng, Z.; Lei, J.; Xiao, Z.; Cao, W.; Cai, Z.; Cheng, W.; Feng, X.; Ping, J. Re-Evaluating Influence of Rocks on Microwave Thermal Emission of Lunar Regolith Using CE-2 MRM Data. *IEEE Trans. Geosci. Remote Sens.* **2022**, *60*, 1–12. [[CrossRef](#)]
34. Meng, Z.; Hu, S.; Wang, T.; Li, C.; Cai, Z.; Ping, J. Passive Microwave Probing Mare Basalts in Mare Imbrium Using CE-2 CELMS Data. *IEEE J. Sel. Top. Appl. Earth Obs. Remote Sens.* **2018**, *11*, 3097–3104. [[CrossRef](#)]
35. Huang, Y.-H.; Minton, D.A.; Hirabayashi, M.; Elliott, J.R.; Richardson, J.E.; Fassett, C.I.; Zellner, N.E.B. Heterogeneous impact transport on the Moon. *J. Geophys. Res. Planets* **2017**, *122*, 1158–1180. [[CrossRef](#)]

36. Fang, T.; Fa, W. High frequency thermal emission from the lunar surface and near surface temperature of the Moon from Chang'E-2 microwave radiometer. *Icarus* **2014**, *232*, 34–53. [[CrossRef](#)]
37. Fa, W. Simulation for ground penetrating radar (GPR) study of the subsurface structure of the Moon. *J. Appl. Geophys.* **2013**, *99*, 98–108. [[CrossRef](#)]
38. Kong, J.A. *Electromagnetic Wave Theory*; EMW Press: Cambridge, UK, 2005.
39. Campbell, B.A.; Carter, L.M.; Hawke, B.R.; Campbell, D.B.; Ghent, R.R. Volcanic and impact deposits of the Moon's Aristarchus Plateau: A new view from Earth-based radar images. *Geology* **2008**, *36*, 135–138. [[CrossRef](#)]
40. Cai, Z.; Lan, T. Lunar Brightness Temperature Model Based on the Microwave Radiometer Data of Chang'e-2. *IEEE Trans. Geosci. Remote Sens.* **2017**, *55*, 5944–5955. [[CrossRef](#)]
41. Amidror, I. Scattered data interpolation methods for electronic imaging systems: A survey. *J. Electron. Imaging* **2002**, *11*, 157–176. [[CrossRef](#)]
42. Hu, G.P.; Zheng, Y.C.; Xu, A.A.; Tang, Z.S. Qualitative Verification of CE-2's Microwave Measurement: Relative Calibration Based on Brightness Temperature Model and Data Fusion. *IEEE Trans. Geosci. Remote Sens.* **2016**, *54*, 1598–1609. [[CrossRef](#)]
43. Hu, G.-P.; Chan, K.; Zheng, Y.-C.; Tsang, K.; Xu, A.-A. Comparison and Evaluation of the Chang'E Microwave Radiometer Data Based on Theoretical Computation of Brightness Temperatures at the Apollo 15 and 17 Sites. *Icarus* **2017**, *294*, 72–80. [[CrossRef](#)]
44. Wei, G.; Byrne, S.; Li, X.; Feng, J.; Siegler, M.A. A New Method to Evaluate and Modify Chang'E-2 Microwave Radiometer Low-Frequency Data Constrained from Diviner Thermal Measurements. *IEEE Trans. Geosci. Remote Sens.* **2022**, *60*, 1–13. [[CrossRef](#)]
45. Yang, F.; Hu, G.P.; Chan, K.L.; Tsang, K.T.; Zheng, Y.C.; Xu, Y.; Yu, L.H.S. A Recalibration Model Based on the Statistical Regression Analysis Method to Align the Microwave Data of Chang'E-1 and Chang'E-2. *IEEE Trans. Geosci. Remote Sens.* **2022**, *60*, 1–11. [[CrossRef](#)]
46. Bandfield, J.L.; Ghent, R.R.; Vasavada, A.R.; Paige, D.A.; Lawrence, S.J.; Robinson, M.S. Lunar surface rock abundance and regolith fines temperatures derived from LRO Diviner Radiometer data. *J. Geophys. Res. Planets* **2011**, *116*. [[CrossRef](#)]
47. Xie, M.; Xiao, Z.; Zhang, X.; Xu, A. The Provenance of Regolith at the Chang'e-5 Candidate Landing Region. *J. Geophys. Res. Planets* **2020**, *125*, e2019JE006112. [[CrossRef](#)]
48. Yue, Z.; Johnson, B.C.; Minton, D.A.; Melosh, H.J.; Di, K.; Hu, W.; Liu, Y. Projectile remnants in central peaks of lunar impact craters. *Nat. Geosci.* **2013**, *6*, 435–437. [[CrossRef](#)]
49. Fa, W.; Jin, Y. A primary analysis of microwave brightness temperature of lunar surface from Chang-E 1 multi-channel radiometer observation and inversion of regolith layer thickness. *Icarus* **2010**, *207*, 605–615. [[CrossRef](#)]
50. Fa, W.; Wiczorek, M.A. Regolith thickness over the lunar nearside: Results from Earth-based 70-cm Arecibo radar observations. *Icarus* **2012**, *218*, 771–787. [[CrossRef](#)]
51. Qiu, D.; Li, F.; Yan, J.; Wang, X.; Gao, W.; Deng, Q.; Guo, X. New view of the Balmer-Kapteyn region: Cryptomare distribution and formation. *Astron. Astrophys.* **2022**, *659*, A4. [[CrossRef](#)]
52. Schreiner, S.S.; Dominguez, J.A.; Sibille, L.; Hoffman, J.A. Thermophysical property models for lunar regolith. *Adv. Space Res.* **2016**, *57*, 1209–1222.